OPTICS

Submicrometer perovskite plasmonic lasers at room temperature

Sangyeon Cho[1,2], Yi Yang[3], Marin Soljačić[3], Seok Hyun Yun[1,2]*

Plasmonic lasers attracted interest for their ability to generate coherent light in mode volume smaller than the diffraction limit of photonic lasers. While nanoscale devices in one or two dimensions were demonstrated, it has been difficult to achieve plasmonic lasing with submicrometer cavities in all three dimensions. Here, we demonstrate submicrometer-sized, plasmonic lasers using cesium-lead-bromide perovskite ($CsPbBr_3$) crystals, as small as 0.58 μm by 0.56 μm by 0.32 μm (cuboid) and 0.79 μm by 0.66 μm by 0.18 μm (plate), on polymer-coated gold substrates at room temperature. Our experimental and simulation data obtained from more than 100 plasmonic and photonic devices showed that enhanced optical gain by the Purcell effect, large spontaneous emission factor, and high group index are key elements to efficient plasmonic lasing. The results shed light on the three-dimensional miniaturization of plasmonic lasers.

INTRODUCTION

Nanoscale lasers have received growing interest for scientific and practical applications. Various types of photonic nanolasers have been demonstrated. For example, planar photonic crystal cavities coupled with semiconductor quantum dots (*1*) or transition metal dichalcogenides (*2*) achieved lasing in the near infrared at cryogenic temperatures. Semiconductor cuboidal and disk lasers with submicrometer sizes were reported in the green (*3*) and red wavelengths (*4*, *5*). While the minimum size of photonic lasers is limited to half the optical wavelength in the laser materials, incorporating metals at the perimeter is a promising route to reduce device size beyond what is possible with only semiconductors and dielectrics (*6*). Metals can support surface plasmon polariton (SPP) modes and can also serve as reflectors for photonic modes enhancing their confinement in the cavity (*7*). For example, metallodielectric lasers supporting high-*Q* photonic modes with subwavelength mode volume sizes were realized with silver-encapsulated semiconductor disks at 1550 nm (*8*).

Among plasmonic lasers, one class known as spaser uses localized SPPs. Since its inception (*9*), narrowband emission from dye-embedded colloidal ensembles (*10*, *11*) has been observed, although lasing of single spaser nanoparticles remains to be seen (*12*, *13*). Recent progress was made with an array of metallic nanopillars supporting plasmonic lattice modes. Coupling with emerging lanthanide-based upconverting emitters (*14*), the lattice nanocavity exhibits continuous-wave laser emission at room temperature. The other class of plasmonic lasers uses propagating SPPs along the interface of a metal and gain material (*15*–*18*). Plasmonic lasing was demonstrated with CdS (*15*, *17*) or GaN (*16*) semiconductor nanowires on top of silver substrates at cryogenic and vacuum conditions. Recently, room temperature plasmonic lasing was demonstrated with GaN nanowires (*18*) on aluminum at 375 nm and CdSe microplates (*6*) with gold at 700 nm. However, almost all the SPP-based plasmonic lasers demonstrated to date have required at least one dimension along cavity resonance to be >1 μm to restrict cavity radiative loss.

Here, we demonstrate full submicrometer plasmonic lasers operated at room temperature using lead halide perovskite (LHP) and gold. LHPs with the form of $APbX_3$ ($A = Cs^+$, $CH_3NH_3^+$, $X = Cl^-$, Br^-, I^-) are promising semiconductor materials for optoelectronic applications (*3*, *19*–*21*). Among different LHPs, cesium lead bromide perovskite ($CsPbBr_3$) is an attractive laser material owing to its long carrier diffusion length (~9 μm) (*22*) and high optical gain (~4000 cm^{-1}) (*23*), as well as solution processability. Using $CsPbBr_3$ submicrometer cubes atop polymer-coated gold substrates, we achieved stable single- and multimode lasing in the air at 2.3 eV (=540 nm) with a narrow laser linewidth of 1 meV (~0.2 nm) using nanosecond optical pumping. By measuring key laser parameters including the Purcell factor, spontaneous emission factor (β), and quantum yield (η), we systematically studied the lasing action of both plasmonic lasers (test) and their photonic counterparts (control). The comparison enabled us to identify and explain a condition where efficient plasmonic lasing becomes possible.

RESULTS

Plasmonic lasing from submicrometer perovskite crystals

We synthesized $CsPbBr_3$ micrometer- and submicrometer-sized crystals using a sonochemistry method (fig. S1) (*24*). The crystals typically have orthorhombic shapes with aspect ratios of 0.5 to 0.9 and a corner curvature of 0.08 μm. The height-to-length ratio can be further reduced down to 0.1 in microplate shapes by adding nonionic surfactants during sonochemical synthesis (*25*). The prepared $CsPbBr_3$ crystals were subsequently transferred onto different substrates: gold (Au) coated with polynorepinephrine (pNE), pNE-coated silicon (Si), and bare silica (SiO_2) (Fig. 1A). $CsPbBr_3$ crystals on the gold substrate form the plasmonic laser group (test), while those on dielectric SiO_2 or Si substrates are photonic counterparts (control).

We first investigated devices with cuboidal crystals fabricated with height-to-length ratios of 0.5 to 0.9. The relatively large aspect ratio is generally more favorable to photonic modes. The quantities of devices in the test and control groups are 30 (Au), 25 (Si), and 45 (SiO_2), respectively. We pumped each device with nanosecond optical pulses at 480 nm (duration, 4 ns; repetition rate, 20 Hz) and recorded output emission spectra at various pump levels (fig. S2A)

[1]Wellman Center for Photomedicine, Massachusetts General Hospital and Harvard Medical School, 65 Landsdowne St., Cambridge, MA 02139, USA. [2]Harvard-MIT Health Sciences and Technology, Massachusetts Institute of Technology, 77 Massachusetts Avenue, Cambridge, MA 02139, USA. [3]Research Laboratory of Electronics, Massachusetts Institute of Technology, 77 Massachusetts Avenue, Cambridge, MA 02139, USA.
*Corresponding author. Email: syun@hms.harvard.edu

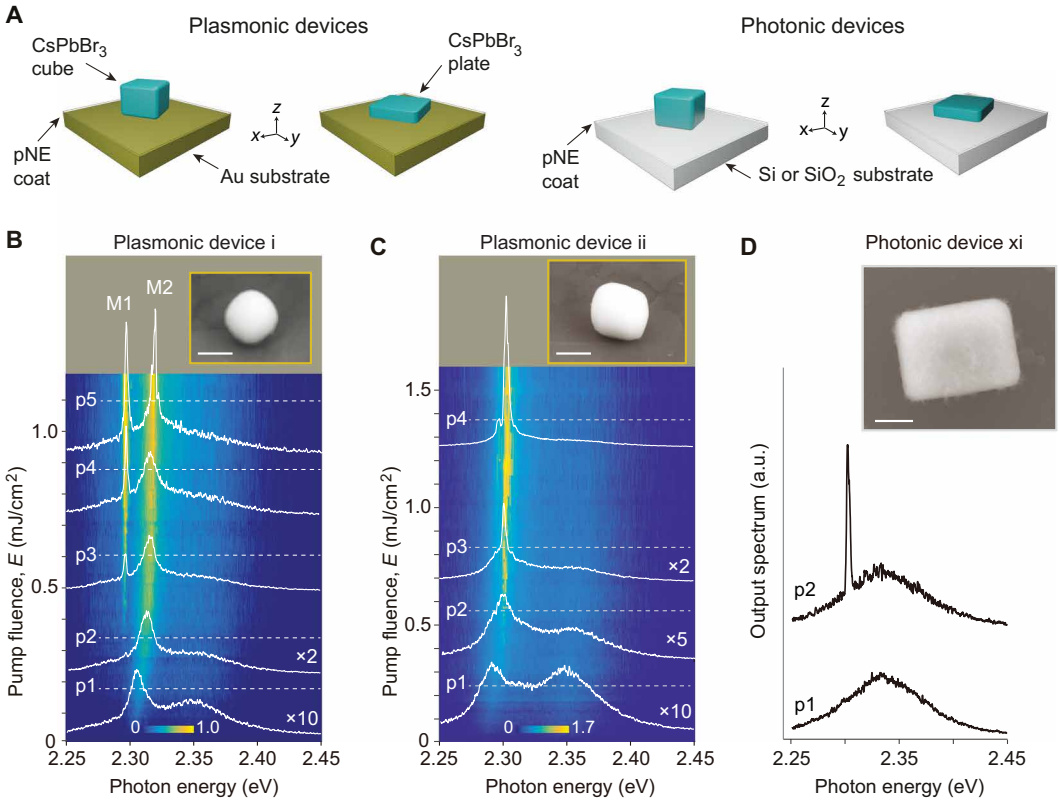

Fig. 1. Plasmonic versus photonic lasers. (**A**) Schematic of plasmonic (pNE-coated Au substrate) and photonic (pNE-coated Si or bare SiO_2 substrates) devices. (**B** and **C**) Single-shot photoluminescence (PL) spectra of the two smallest plasmonic lasers [device i, $L = 0.57$ μm (B); device ii, $L = 0.61$ μm (C)] and their line cuts at various pump fluences. Two lasing modes in device i are denoted by M1 and M2. (**D**) Single-shot PL spectra from a photonic device xi ($L = 1.3$ μm) at pump levels below (p1) and above (p2) thresholds. Scale bars, 500 nm. a.u., arbitrary units.

below and above the lasing threshold by using custom-built hyperspectral optical microscopy. We marked each device's location on the Si substrates by pump laser irradiation at high fluence (fig. S2B). The devices were then imaged with scanning electron microscopy (SEM; resolution, 1.4 nm) for analyzing their shape and size. We calculated the effective device side length, $L = \sqrt{S}$, where S is the device area determined from top-view SEM images. The device height was determined from SEM images taken at sample tilt angles of 45° and 0° from the surface normal.

Many plasmonic devices with full submicrometer sizes demonstrated single-mode or multimode lasing. The smallest plasmonic laser (Fig. 1B, inset) had $L = 0.57$ μm (device i; 0.56 μm by 0.58 μm by 0.32 μm for x, y, and z directions). This device exhibited two lasing modes, M1 and M2 (Fig. 1B), above the threshold fluence. M1 reached lasing first, followed by M2. The second smallest device (device ii; 0.75 μm by 0.49 μm by 0.3 μm; $L = 0.61$ μm) showed single-mode lasing (Fig. 1C, inset). Below the lasing threshold, the plasmonic devices exhibited multiple fluorescence peaks in their photoluminescence (PL) spectra. Figure 2 shows the emission spectra of various other plasmonic devices with submicrometer to micrometer sizes. The 10 smallest plasmonic lasers are denoted by i to x.

By contrast, none of the photonic devices on the dielectric substrates showed lasing even at the maximum power fluence level before optical damage occurs to the gain materials. All lasing photonic devices were measured to have $L > 1.2$ μm, at least 10 times larger in volume than the smallest plasmonic device. Figure 1D shows a representative photonic laser with $L = 1.3$ μm. The shapes and output spectra of other photonic lasers are shown in fig. S3. The photonic devices below the threshold showed typical broad fluorescence spectra, with the sharp peaks observed in the plasmonic devices.

Modal analysis and finite element method simulation

The multiple emission peaks of the two submicrometer plasmonic devices, i and ii, were analyzed using Lorentzian fitting (fig. S4). A sharp reduction of the full width at half maximum (FWHM) of the PL peaks occurs above lasing threshold (Fig. 3, A and B). The smallest FWHM at the threshold is about 2.4 meV (~0.7 nm) and 2.2 meV (~0.5 nm) for M1 and M2 in device i, respectively, and 1 meV (~0.2 nm) in device ii. Both the linewidth narrowing and polarization state in the x-y plane changes (Fig. 3C) are indications of lasing. We reconstructed stimulated emission profiles of M1 and M2 by subtracting emission profiles taken just below their lasing thresholds from emission profiles taken above the thresholds (fig. S2C). From the images, M1 mode appears to be a Fabry-Perot (FP) mode, and the M2 mode is a whispering gallery mode (WGM) (Fig. 3D).

We numerically calculated the two eigenmodes (COMSOL Multiphysics) in device i. The spatial mode profiles agreed with the measurement (Fig. 3E). Both modes are hybrid resonances because their electric fields are concentrated inside the gap region but have considerable energy in the $CsPbBr_3$ crystal (Fig. 3E). The fraction of modal energy inside the 5-nm-thick gap region is about 5% for M1 and 30% for M2 (Fig. 3E). Conceptually, these resonances can be

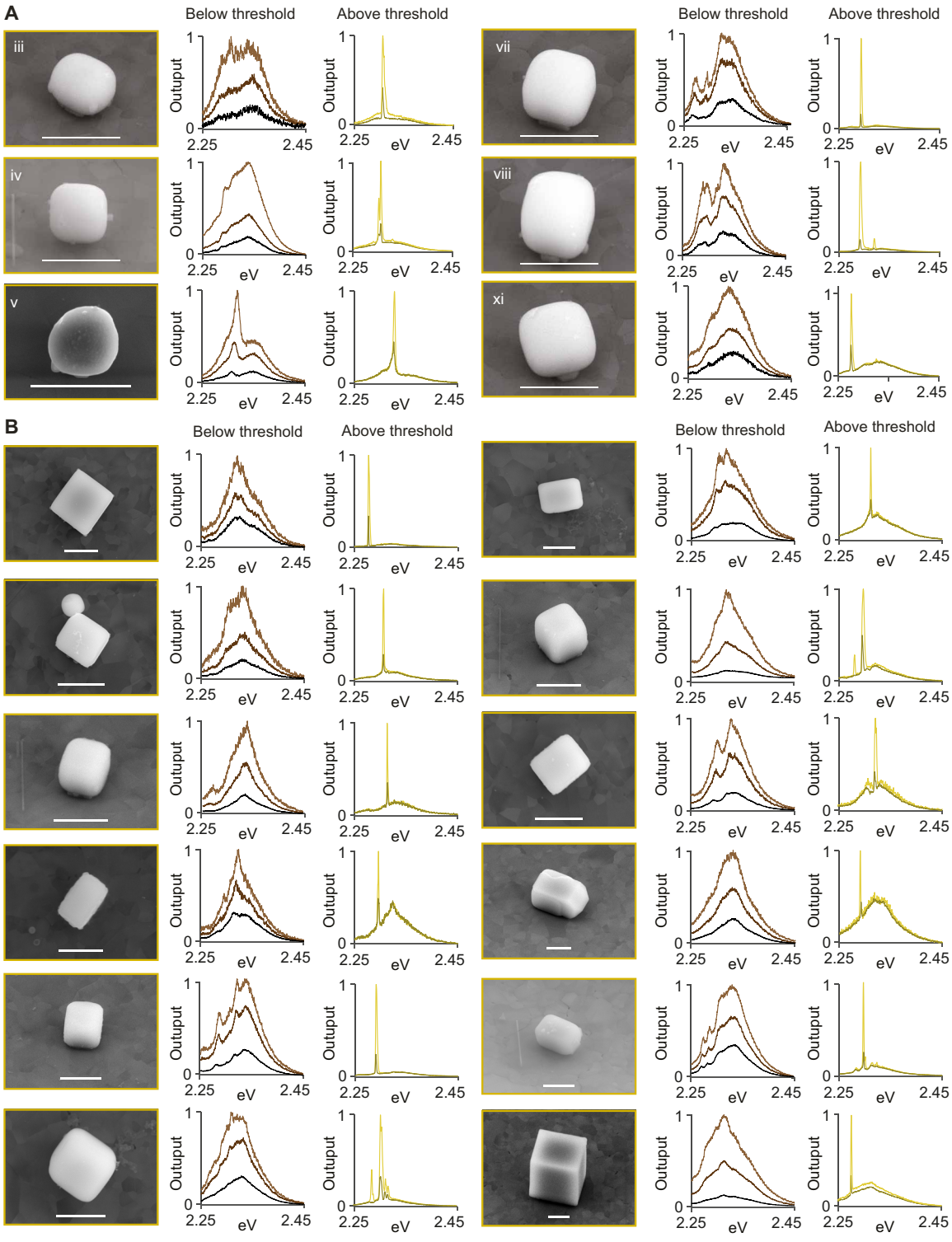

Fig. 2. Shape and spectra of plasmonic laser devices. (**A**) Submicrometer devices (devices iii to xi). (**B**) Microscale devices ($L > 1$ μm). For each device, (left) a representative SEM image, (middle) fluorescence spectra at pump energy E of 0.1 (black), 0.4 (dark brown), and 0.8 (brown) times the threshold E_{th}, respectively, and (right) lasing spectrum above threshold at E= 1.2 (dark yellow) and 2.5 (yellow) times E_{th}, respectively, are displayed. Scale bars, 1 μm.

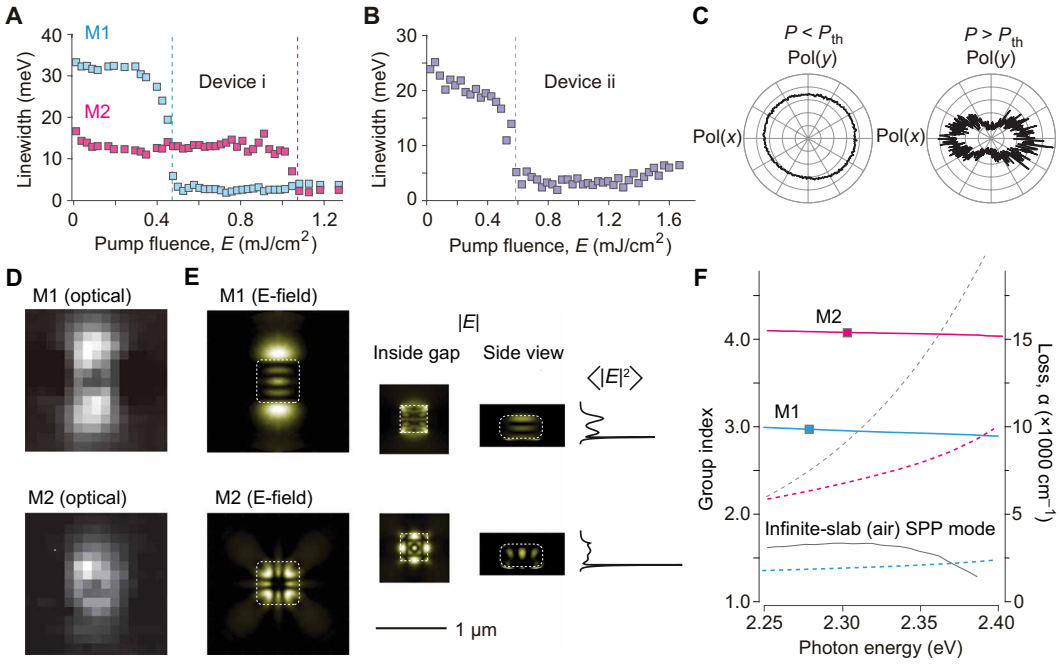

Fig. 3. Emission spectra and energy profiles. (**A** and **B**) Measured spectral linewidth of device i (A) and device ii (B) at different pump fluences. Linewidth reduction occurs at lasing threshold (dashed lines). (**C**) Polar plots showing the polarization states in the *x*-*y* plane of emission below the threshold and above the threshold. (**D**) Measured wide-field images of the stimulated emission of device i. (**E**) Field (|*E*|) and energy ($|E|^2$) profiles of the calculated cavity modes, revealing the FP and whispering gallery nature of the two hybrid plasmonic modes in device i. (**F**) Group refractive indices (solid lines) and absorption loss coefficients (dashed lines) of the M1 (cyan) and M2 (magenta) modes in device i, in comparison to an infinite-slab SPP mode (gray).

understood as the surface plasmons of a planar multilayer metal-dielectric closed system restricted to specific quantized wave vectors determined by the device sizes (*26*). The quality factors (Q_m) of the modes were 61 (M1) and 41 (M2). We also simulated the plasmon dispersions of such closed systems, where the $CsPbBr_3$ layer is infinitely extended in the *x* and *y* directions (fig. S5). From the dispersion, the group indices n_g of the two modes are 2.95 (M1) and 4.1 (M2), and their propagation losses α are 1800 cm^{-1} (M1) and 5800 cm^{-1} (M2) (Fig. 3F). In the simulation of a photonic device with the same size as device i but with a silicon, instead of a gold, substrate, we found two photonic modes with $Q_m \approx 90$ and 38, respectively, and $n_g \approx 2.5$ (fig. S5E). For this submicrometer ($L = 0.57$ μm) device size, the plasmonic cavity modes (M1 and M2) have similar quality factors as these photonic cavity modes. This is primarily because the higher n_g of the plasmonic modes results in stronger boundary reflection compensating the metallic absorptive loss. The similar quality factors indicate that the plasmonic modes are more efficient to reach the lasing threshold compared to the photonic modes at the given gain material.

Laser characteristics and analytical models

The pump fluence at the lasing threshold, E_{th}, was measured from each device in the three experimental groups. Figure 4A plots the result as a function of the effective device side length *L*. Regardless of *L*, the lasing thresholds were similar across all three groups. The photonic devices on both Si and SiO_2 substrates have similar thresholds. This similarity is partly due to oxide layers formed on the Si substrates but mainly because the distribution of the lasing photonic modes is shifted away from the high-index substrates. In the plasmonic test group, we compared E_{th} at three different spacer thicknesses of

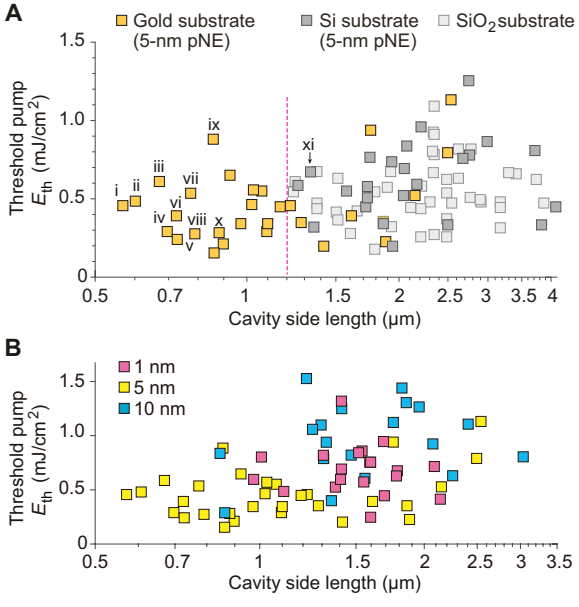

Fig. 4. Lasing thresholds. (**A**) Threshold pump fluence E_{th} measured from individual lasers: 30 plasmonic devices on gold (yellow), 25 photonic devices on Si (dark gray), and 45 photonic devices on SiO_2 substrates (light gray). Ten submicrometer plasmonic lasers are labeled as i to x. One photonic laser xi is marked (Fig. 1D). (**B**) Measured threshold pump fluence of plasmonic lasers fabricated with a different pNE layer thickness of 1, 5, or 10 nm. The 5-nm thickness produces lasing with the smallest device size and lowest mean threshold energy.

1, 5, and 10 nm, respectively (Fig. 4B). The thickness of the pNE spacer of 5 nm led to the smallest lasers, which is consistent with previous observations (*15*).

We studied laser dynamics with a three-level rate equation model (*27*). In this model, the threshold pump absorption rate P_{th} per volume V at frequency ω_0 is given by $P_{th}V = \omega_0/Q_m\beta_m\eta + F_{tot}\rho_{tr}V(1-\beta_m\eta)/\tau_s\eta$ (note S1), where β_m is the spontaneous emission factor of the lasing mode m, η is the quantum yield of the gain medium, F_{tot} is the total enhancement factor of emission, ρ_{tr} is the number of carriers needed to reach transparency in the gain medium, and τ_s is the radiative lifetime. For $CsPbBr_3$ microcrystals, the first term relating to cavity loss is dominant to the second term, which is related to transparency or population inversion in the gain medium (note S1). Thus, the equation can be simplified as $P_{th}V \approx \omega_0/Q_m\beta_m\eta$. To reach the lasing threshold, three parameters in the denominator are important: quality factor Q_m of the lasing mode, the spontaneous emission factor β_m of the lasing mode, and the quantum yield η. Our finite element method (FEM) results above predicted similar Q_m for the plasmonic and photonic devices. Below, we show that compared to the photonic devices, the plasmonic devices actually offer higher β_m and η, essential for lasing at submicrometer V.

We used both laser emission and transient spectroscopy data to measure these laser parameters. First, we extracted β_m of the lasing mode from the PL emission spectra of the plasmonic devices at a low pump fluence at 0.2 mJ/cm^2 (Fig. 5A). Using an analytical ray tracing model (*17*, *28*), we calculated the number of cavity modes, N, within the gain bandwidth (Materials and Methods) to be between 3 and 6, in agreement with experimental data (fig. S6). For the plasmonic devices, we obtained β_m by decomposing their PL spectra into N Lorentzian peaks and a broad background fluorescence curve for uncoupled emission (fig. S4, A and D). The β_m values in the plasmonic devices increase from 0.05 to 0.35 as the device size decrease from 1.3 to 0.6 μm. β_m in the photonic devices cannot be inferred from their PL spectra because of the lack of multiple resonant peaks (fig. S4F).

The PL intensity in the plasmonic devices was substantially higher than the photonic devices at the same effective pump fluence (~0.2 mJ/cm^2) below the threshold (Fig. 5B). We calibrated the brightness with respect to the fluorescence from a batch of relatively large $CsPbBr_3$ microcrystals (>5 μm) synthesized with the same method and placed on 5-nm-thick pNE-coated Si or SiO_2 substrates. Using an objective lens with a numerical aperture (NA) of 0.5, we measured up to 40 times brighter fluorescence from submicrometer plasmonic devices compared to the reference crystals. To understand this large difference, we performed a full-wave simulation of a $CsPbBr_3$ microcrystal with L = 0.57 μm (equivalent to device i). The ratio of total fluorescence collected by the 0.5 NA objective lens, or the collection efficiency, was 0.44, 0.31, and 0.2 for the case of Au, Si, and SiO_2 substrates, respectively (fig. S5F). The relatively small difference supports that the 40-fold brightness is mostly due to an enhanced quantum yield in plasmonic devices. Resonant cavity modes, however, have more pronounced asymmetric emission patterns toward the dielectric substrates and several-fold lower collection efficiency in the vertical direction (fig. S5, G and H) (*29*). Using an integrating sphere, we measured the intrinsic quantum yield (η_{int}) of the reference crystals to be ~0.015 (see Materials and Methods). The quantum yield η of

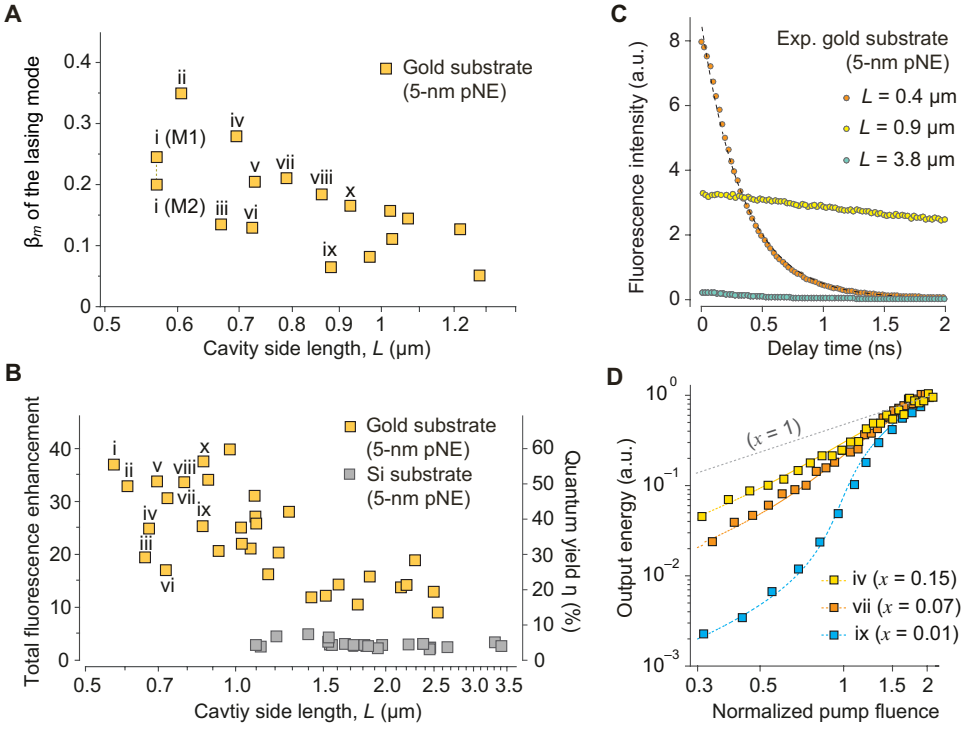

Fig. 5. Laser characteristics. (**A**) Extracted β-factor of the lasing modes for the plasmonic devices (yellow squares). (**B**) Measured fluorescence enhancement (10 to 40 times) and the associated quantum yields η of the plasmonic (yellow) and photonic (gray) devices. (**C**) Time-resolved PL decay (circles) of three $CsPbBr_3$ plasmonic devices and double-exponential fits (dashed lines). The 0.4-μm-sized device exhibits enhanced fluorescence intensity and accelerated decay rates. (**D**) Measured (squares) light-in-light-out curves of three plasmonic devices iv (β_m = 0.28, η = 0.37), vii (β_m = 0.21, η = 0.46), and ix (β_m = 0.06, η = 0.38) and theoretical fits (dashed lines; see note S1B).

the gain crystals in the plasmonic devices was enhanced by 10 to 40 times, ranging from 0.15 to 0.6. The Purcell factors (*30*, *31*) calculated from the measured β_m and η agreed with the values obtained from a numerical simulation of the rate equation model (fig. S7).

We verified the Purcell-induced emission enhancement using time-resolved spectroscopy. Figure 5C shows representative fluorescence decays of $CsPbBr_3$ crystals with three different sizes, placed on pNE-coated gold substrates (Fig. 5C). Table 1 summarizes various fluorescence decay parameters determined from $CsPbBr_3$ crystals on gold or silicon substrates. The Purcell factors measured from the fluorescence decay data were greater than 20 for $CsPbBr_3$ crystals ($L < 3$ μm) on gold (fig. S8). This enhancement factor is consistent with those obtained from the PL measurement in Fig. 5B.

The light-in-light-out (L-L) curve is another crucial indicator of lasing. Specifically, the presence of a nonlinear kink at the threshold in an L-L curve is determined by a parameter $x = \beta_m\eta$ (Fig. 5D and note S1) (*32*). The extracted x parameters are comparable with the product of the spontaneous emission factor β_m and quantum yield η values that were obtained independently in Fig. 5 (A and B).

Plasmonic and photonic devices made of $CsPbBr_3$ plates

Having analyzed the laser devices using cuboidal crystals, we investigated plate-shape $CsPbBr_3$ crystals fabricated with height-to-side ratios of 0.1 to 0.4. Figure 6A shows measured pump threshold fluences for all three device groups (Au for plasmonic, Si and SiO_2 for photonic). The smallest plasmonic device that lased had $L = 0.6$ μm. None of the plasmonic devices smaller than $L = 0.5$ μm reached lasing. By comparison, the smallest lasing photonic device had $L = 1.7$ μm. Figure 6B displays the output spectra from a plasmonic device (xii) with a size of 0.79 μm by 0.66 μm by 0.18 μm at various pump fluences below and above the threshold of 0.7 mJ/cm^2. The numerical simulation found a few plasmonic hybrid modes in the gain bandwidth. The highest Q-factor mode had $Q_m \approx 26$ and 15% of energy inside the gap (fig. S9). Figure 6C shows the broadband fluorescence spectra from a photonic device with $L = 1.2$ μm on a Si substrate, which failed to reach lasing at pump fluences close to a material damage threshold of ~2 mJ/cm^2.

To investigate the spatial profiles of cavity modes, we used two-photon excitation microscopy and mapped PL emission as excitation light (920 nm, 150 fs, 80-MHz repetition) was raster-scanned in transverse cross sections at different depth positions of devices. Because the excitation photon energy (1.35 eV) is below the bandgap energy (2.38 eV) of the gain medium, charge carriers are generated at the focal plane via two-photon absorption with an axial resolution of ~2 μm given by the NA (0.9) of the excitation beam (*33*). Since the absorption is more or less uniform in the gain medium, any difference in the output PL intensity is primarily due to the difference in the Purcell effect at the focus. Figure 7 (A to D) shows two-photon images of various devices with sizes of 2 to 5 μm. All the plasmonic devices built on 5-nm-thick pNE-coated gold substrates show the maximum intensity when the focal planes were at crystal-gold interfaces (Fig. 7E). By comparison, the maximum intensity appeared 0.5 to 1.5 μm away from crystal-gold interfaces when the thickness of the pNE coating was 20 nm instead of 5 nm (Fig. 7F). The 20-nm pNE spacer is thick enough to suppress plasmonic effects (*31*), making these devices effectively photonic devices. Considering the same geometry except for the additional dielectric gap thickness by 15 nm, the difference in the maximum intensity plane indicates the difference in the axial mode profile (*34*, *35*). For pure photonic devices built on SiO_2 and Si substrates, the maximum intensity planes were also located at 0.5 to 1.5 μm above the substrate, approximately in the middle of the gain crystals (Fig. 7G). This result supports the enhanced Purcell effect in the plasmonic devices in the vicinity of the gold substrates with 5-nm dielectric layers.

Polarization state and stability of laser emission

Photonic lasers with the highest Q-factors in thin microcube cavities typically have transverse-electric (TE) modes with the electric fields predominantly parallel to their substrates, but plasmonic hybrid modes are transverse-magnetic (TM) mode–like with the electric field predominantly orthogonal to the gain-metal interface. To confirm this distinct feature, we measured far-field emission images of laser devices through a linear polarizer (Fig. 8A). The sample substrates were tilted by 85° so that emission from both the side and top surfaces of the cavities is captured. For plasmonic lasing, the output emission is expected to be largely polarized along the out-of-plane (~z axis), whereas for photonic lasing, the output is supposed to be polarized along the in-plane (x axis) (Fig. 8B). Figure 8 (C and D) shows the stimulated emission images (below-threshold images subtracted from images above threshold; see fig. S2C) of four plasmonic

Table 1. Measured fluorescence decay parameters. TCSPC, time-correlated single photon counting.

	Plasmonic $CsPbBr_3$ on pNE-gold			Photonic $CsPbBr_3$ on pNE-Si		
	$L = 0.4$ μm	$L = 0.9$ μm	$L = 3.8$ μm	$L = 0.7$ μm	$L = 2.4$ μm	$L = 4.3$ μm
τ_1 from TCSPC	0.7 ns	1.2 ns	2.6 ns	4.1 ns	2.5 ns	3.2 ns
τ_2 from TCSPC	–	–	18 ns	–	5.8 ns	5.6 ns
A_1 from TCSPC	1	1	0.76	1	0.62	0.68
A_2 from TCSPC	–	–	0.23	–	0.38	0.32
τ_{tot} measured	0.7 ns	1.2 ns	3.3 ns	4.1 ns	3.8 ns	3.7 ns
F_{tot} measured	50	20	1	0.5	5	1
η measured	0.4	0.1	0.015	0.007	0.075	0.015
τ_s computed	88 ns	240 ns	220 ns	270 ns	250 ns	250 ns
τ_{nr} computed	0.71 ns	1.2 ns	3.3 ns	4.1 ns	3.8 ns	3.7 ns

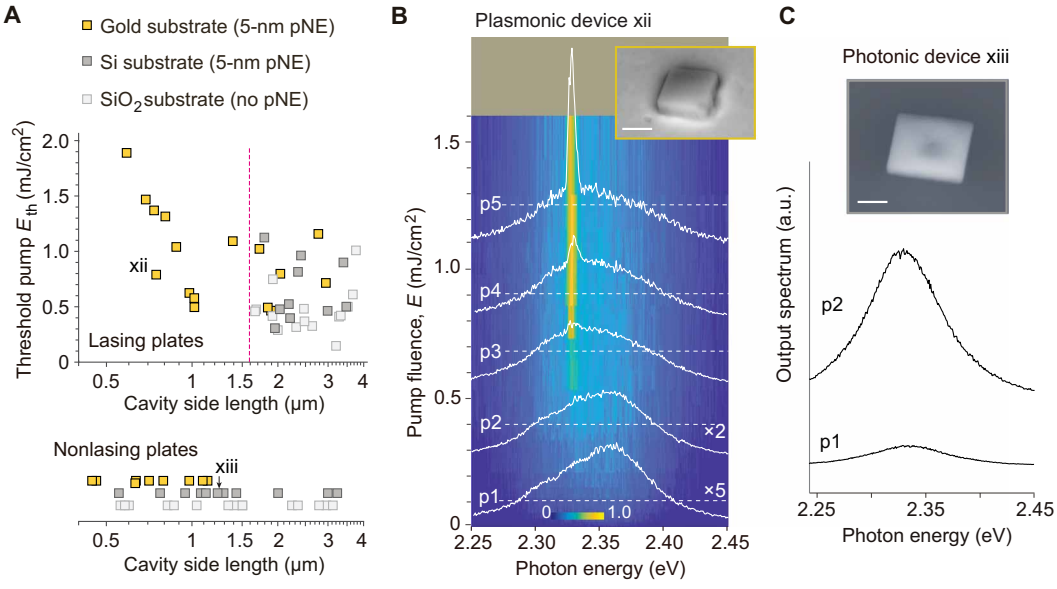

Fig. 6. Plasmonic lasing of submicrometer $CsPbBr_3$ microplates. (**A**) Threshold pump fluence E_{th} measured from individual lasers: 25 plasmonic devices on gold (yellow), 24 photonic devices on Si (dark gray), and 30 photonic devices on SiO_2 substrates (light gray). Nonlasing devices are also shown. (**B**) Single-shot PL spectra of a plasmonic laser (device xii, $L = 0.72$ μm, thickness of 0.18 μm) at various pump fluences. (**C**) Single-shot PL spectra from a nonlasing photonic device xiii ($L = 1.2$ μm) at low (p1 = 0.2 mJ/cm^2) and high (p2 = 2 mJ/cm^2) pump levels. Scale bars, 500 nm.

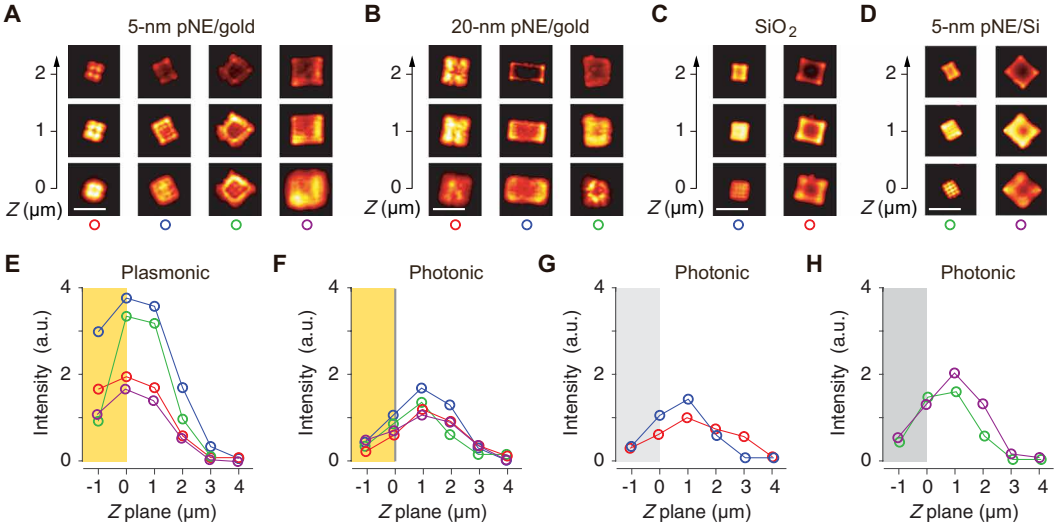

Fig. 7. Two-photon excited PL intensity profiles of plasmonic and photonic devices. (**A** to **D**) Two-photon excitation PL images at different focal plane position (*Z*) from the substrates for various $CsPbBr_3$ microplates on different substrates: (A) 5-nm pNE-coated gold, (B) 20-nm pNE-coated gold, (C) SiO_2, and (D) 5-nm pNE-coated Si. Scale bars, 5 μm. (**E** to **H**) Plane-integrated PL intensity measured from the images in (A) to (D). The color of the data points (circles) in (E) to (H) denotes the different devices in (A) to (D).

devices on 5-nm-thick pNE-coated gold substrates and four photonic devices on Si substrates. For the plasmonic devices, out-of-plane polarization components were four to five times greater than in-plane polarizations (Fig. 8E). The opposite trend was observed for the photonic devices (Fig. 8E). Three of four photonic devices had in-plane polarization about fourfold greater than out-of-plane polarization. One device (purple circle) exhibits nearly equal intensity in both polarizations, probably because of the FP resonance in the *y* axis (Fig. 8B). This result evidences that the lasing modes of plasmonic devices are TM-like plasmonic hybrid modes.

Both plasmonic and photonic lasers were stable over 10,000 pump pulses (20-Hz pulse rate) (Fig. 8, F and G). Pulse-to-pulse wavelength fluctuations were measured to be 0.12 nm for plasmonic devices, better than 0.28 nm for photonic devices on silicon substrates and 0.40 nm for glass substrates. The reason for these differences is not fully understood but may be due to reduced charge accumulation (*36*). We expect that the heating of $CsPbBr_3$ microcrystals during laser oscillation is nearly the same regardless of substrate materials. The thermal conductivity of $CsPbBr_3$ is about 0.4 mm^2/s (*37*) and that of bulk gold is 127 mm^2/s. During 4 ns, the heat diffusion distance

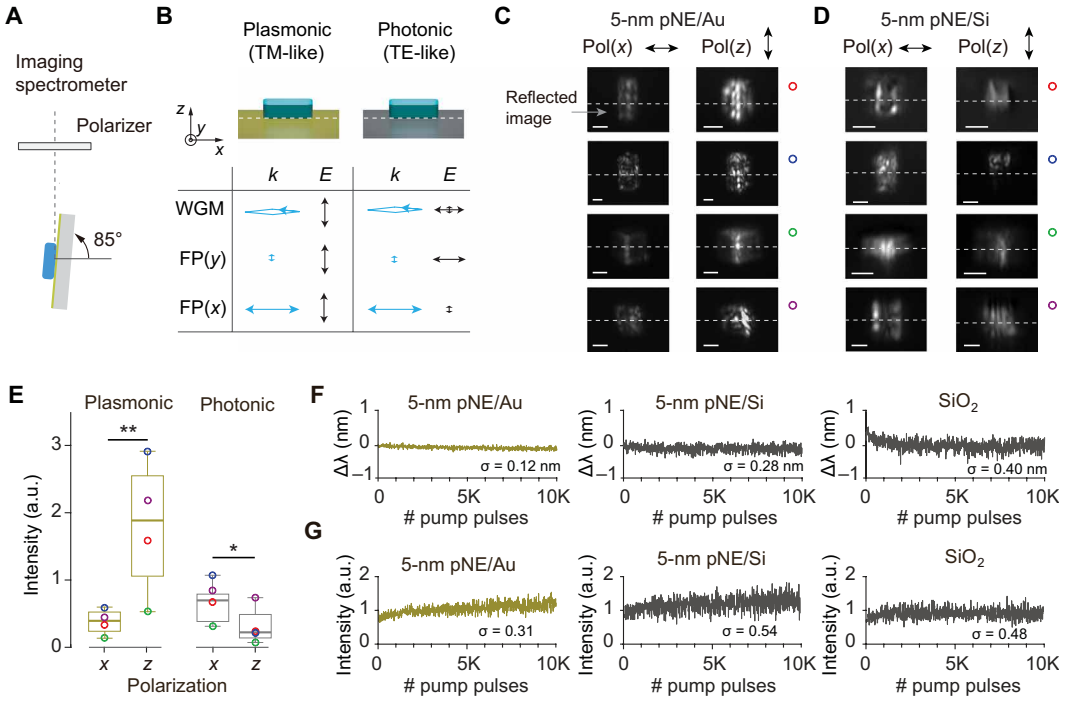

Fig. 8. Polarization state and stability of laser emission. (**A**) Schematic of the measurement setup. (**B**) Output polarization states of different cavity modes. The reference frame applies to both top and bottom panels (table). (**C** and **D**) Reconstructed stimulated emission profiles of in-plane (*x*) and out-of-plane (*z*) polarizations for various $CsPbBr_3$ microcubes on different substrates. Scale bars, 2 μm. Images below dashed lines result from reflection from the substrates. (**E**) Average stimulated emission intensity of the devices (marked by colored circles) displayed in (C) and (D). *$P < 0.5$ and **$P < 0.05$ according to paired *t* test. (**F**) Stability of the lasing wavelength and (**G**) output intensity for three different types of devices over 10,000 pump pulses at 20-Hz repetition with pump fluence at twice the laser threshold (~1 mJ/cm^2). The plotted traces are mean values of 10 samples for each type.

is only 40 nm in $CsPbBr_3$ and 710 nm in gold. Therefore, the temperature of $CsPbBr_3$ microcrystals during laser buildup and oscillation is nearly the same for both plasmonic and photonic devices (fig. S10).

DISCUSSION

Our systematic study of the lasing actions in both plasmonic and photonic devices allowed us to identify a regime where efficient plasmonic lasing becomes possible. Figure 9 illustrates the regime from the perspective of gain, in which the threshold carrier density ρ_{th} is plotted for the three experimental groups. The theoretically calculated curves (solid and dashed lines) are based on $\rho_{th}V \approx \omega_0\tau_s/Q_m\beta_m F_{tot}$ (note S1). The experimental ρ_{th} data (squares) were drawn from measured E_{th} values (fig. S11 and Materials and Methods). The benefit of high group indices and Purcell factors in the plasmonic devices outweighs the metallic absorptive loss, resulting in a net decrease of the lasing threshold. The regime for efficient plasmonic lasing is indicated by a shaded yellow region in Fig. 9.

Experimentally realizing this regime for submicrometer plasmonic lasing, however, should not be taken for granted because the gain medium must be able to produce the threshold carrier density. Two properties of the $CsPbBr_3$ seemed to have played a critical role, which are a low carrier loss at high density and a long carrier diffusion length. From the material's perspective, the maximal attainable ρ (proportional to optical gain) is limited by various loss mechanisms, such as Auger recombination and heat-induced material damage. In $CsPbBr_3$ near the lasing threshold, carrier density ρ exceeds the

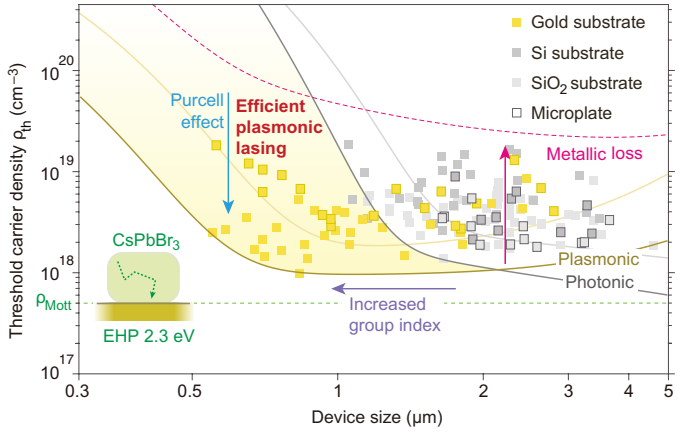

Fig. 9. Efficient plasmonic lasing. As the laser device size decreases, a regime (yellow region) that makes plasmonic lasing more efficient than photonic lasing emerges. The solid curves indicate the calculated threshold carrier density for our plasmonic (brown solid line) and photonic (gray solid line) lasers, respectively. Our experimental data are plotted (squares; calculated from Fig. 4A for microcubes and Fig. 6A for microplates). The metallic loss (magenta upward arrow) increases the lasing threshold (pink dashed curve), which is compensated by the Purcell effect (cyan downward arrow). The higher group index of plasmonic modes reduces the radiative loss for a given device size (purple leftward arrow). Inset: Device schematic illustrating the migration of charge carriers in the strongly pumped EHP state above the Mott transition density (ρ_{Mott}; horizontal dashed green line) of optically pumped $CsPbBr_3$.

Mott transition density ρ_{Mott} (dashed green line in Fig. 9) and reaches 10^{18} to 10^{19} cm^{-3}, forming electron-hole plasma (EHP) (note S2) (*38*). At $\rho = 10^{19}$ cm^{-3}, a high gain coefficient of 4000 cm^{-1} has previously been reported (*23*). Gain coefficients under strong pumping conditions can be much greater than absorption coefficients at the same wavelength without pumping (*23*, *38*, *39*). This is because the gain and absorption spectra are altered at the high concentration of charge carriers in the EHP state (note S3) via various nonlinear processes, such as the EHP plasmon-coupled stimulated emission (*38*), bandgap renormalization in the EHP state (*40*, *41*), suppressed cooling bottleneck under the resonant pumping (*23*), and slow large polaron formation (*42*, *43*). The gain coefficients of $CsPbBr_3$ are comparable to those of the state-of-the-art III-V semiconductors, such as InGaN quantum wells in the green wavelength range (*44*), and II-VI semiconductors, such as CdSe in the far-red wavelength range (*45*). The diffusion length of charge carriers in $CsPbBr_3$ exceeds 9 μm (*22*, *46*). This large diffusivity allows the charge carriers created over the entire device volume to migrate in the gain medium and increase the chance of interaction with plasmonic lasing modes (*7*), undergoing Purcell-enhanced radiative recombination (Fig. 9, inset).

The $CsPbBr_3$-on-gold lasers that we demonstrated are operated in the efficient plasmonic lasing regime. Compared to previously reported visible plasmonic lasers (table S1), the largest dimension of 580 nm of device i represents about 2-fold reduction over II-VI lasers (*6*, *17*) and 20-fold reduction over organic-inorganic hybrid perovskites (*47*). The pump fluence and pulse energy are comparable to those of state-of-the-art plasmonic devices (fig. S12) (*6*, *14*, *17*). In a recent paper, $CsPbBr_3$ submicrometer cubes formed on sapphire substrates using a spin-coating method showed an eightfold higher quantum yield than those formed on glass substrates and were used to achieve lasing in Mie-resonant photonic devices as small as 310 nm in size, twofold smaller than our devices (*3*). Our work shows that, for given gain materials, plasmonic modes could lead to further miniaturization. Although the specific fabrication method does not render a simple path to form plasmonic devices on gold substrates, efforts to use the ongoing innovations in dielectric cavities (*48*, *49*) and gain materials (*50*) in the plasmonic configuration would be worthwhile. These improvements may further miniaturize plasmonic nanolasers toward the deep subdiffraction limit.

Last, both the gain medium and dielectric gap material in our devices were fabricated entirely using solution-based chemistry in room temperature, instead of conventional epitaxial or sputtering processes in a high-temperature vacuum. This unique fabrication method holds promise for adding functional organic molecules (*51*) and tuning the laser wavelength by postsynthetic anionic exchange of the material compositions (*52*).

MATERIALS AND METHODS

Fabrication of laser devices

For producing $CsPbBr_3$, CsBr and $PbBr_2$ were dispersed at an equal saturating concentration (typically 75 mM each) in *N*,*N*-dimethylformamide (DMF) in a vial. The vial was sonicated at 20 to 80 kHz in a bath-type ultrasonicator or a tip ultrasonicator in room temperature. After 2 to 3 min of ultrasonication, single-phase $CsPbBr_3$ micrometer- and submicrometer-sized crystals in cuboidal shapes are spontaneously formed. For the synthesis of microplates, polysorbate 80 (0.1%, v/v) was added before sonication. For pNE coating, 2 mg of DL-norepinephrine hydrochloride was mixed with tris-HCl buffer (pH 8.5). A polycrystalline Au film–coated substrate (Platypus) was placed in this solution at room temperature. An incubation time of 2.5 hours produces a 5-nm-thick pNE layer on the gold. The coated film was cleaned and dried under a stream of N_2 flow. Last, the prepared $CsPbBr_3$ crystals were drop-casted on pNE-coated Au substrates. For photonic devices, pNE-coated Si substrates or uncoated SiO_2 substrates were used.

Material characterization

The complex refractive index was measured from variable angle spectroscopic ellipsometry data measured over 55° to 75°C in steps of 5°C (J.A. Woollam V-VASE32). The spectral range was from 300 to 620 nm. The data fitting was initiated with the Cauchy model at the transparent region and completed by the Gaussian oscillator model. For powder x-ray diffraction, data over 2θ angles from 10° to 60° were collected using a PANalytical X'Pert PRO high-resolution x-ray diffraction system with a CuKα irradiation source. For SEM and energy-dispersive x-ray (EDX), samples were transferred onto a chipped Si wafer by drop-casting and imaged using a Zeiss Merlin high-resolution SEM equipped with an EDX detector operated at 15 kV. For TEM, samples were drop-casted onto a grid (Ted Pella), and images were acquired using a FEI Tecnai Multipurpose TEM at 120 kV. The illumination beam was expanded to avoid sample damage. Atomic force microscopy images were acquired using the NanoScope IV Scanning Probe Microscope (Veeco Metrology Group) in a tapping mode. Spectroscopic ellipsometry was demonstrated at the Harvard Center for Nanoscale Systems. All other measurements were performed at the Massachusetts Institute of Technology (MIT) Center for Material Science and Engineering.

Laser characterization

The samples are placed in a homebuilt epifluorescence microscopy setup (fig. S2A). The pump light source was an optical parametric oscillator (Opotek HE 355 LD) tuned to 480 nm with a repetition rate of 20 kHz and a pulse duration of 4 ns. The pump light in a circular polarization state was focused to a single device via a 0.5 NA, 50× air objective lens (Nikon) with an FWHM beam width of ~25 μm. The output emission from the device is collected by the objective lens, passed through a dichroic mirror and a dichroic filter, and split to an electron multiplication charge coupled device (EMCCD) camera (Luca, Andor) for wide-field imaging and to a grating-based EMCCD spectrometer (Shamrock, Andor) with a spectral resolution of ~0.1 nm. For absolute quantum yield measurement, we used a continuous-wave laser at 491 nm (Cobolt Calypso) for excitation. For time-resolved PL measurements, we used a picosecond laser (VisIR-765, PicoQuant), which was frequency-doubled to 382 nm for excitation, a single-photon avalanche photodiode (Micro Photonics Devices) with a response time of 50 ps, and a time-correlated single-photon counting board (TimeHarp 260, PicoQuant) with a resolution of 25 ps. For polarization measurement, the linear polarizer was placed on the detection path in the setup (fig. S2A), and the polarizer angle was rotated by using a motorized rotation mount. For two photon-excited PL imaging, a laser scanning intravital microscope (IVIM Technology) with femtosecond excitation laser (920 nm, 150 fs, 80-MHz repetition) was used. All optical measurements were conducted at room temperature.

FEM simulation

The eigenmodes and field profiles of the submicrometer lasers were numerically simulated with a commercial finite-element solver

COMSOL Multiphysics with geometries as close to the shapes found by SEM as possible. The Purcell factors were obtained by calculating the spontaneous emission rates of vertical-oriented dipoles inside the gap region.

The number of resonance modes

The resonance condition for cavity modes is given by $(m_x + m_y)\lambda = 2n\left[\left(L + \frac{a}{2}\right)\cos\theta + \left[\left(L - \frac{a}{2}\right)\sin\theta\right]\right.$, where m_x and m_y are integers, $N = m_x + m_y$, n is the effective refractive index of the modes in the crystal, and θ is a beam angle to the surface normal within a range between θ_c and $\pi/2 - \theta_c$, where $\theta_c = \sin^{-1}(1/n)$ is the critical angle for total internal reflection (*28*). The circles in fig. S6 (A and C) were generated for several different aspect ratios (a/L = 1, 1.05, 1.1, 1.15, and 1.2). From the spread of these simulation data, the variability observed in the experimental data may be attributed to small differences in the aspect ratio and shape of the gain crystals in the devices. An approximation solution of the cavity resonance condition has been derived (*17*): $N \approx \text{Round}\left[32\, n_g n \frac{\delta\nu}{\nu}\left(\frac{L}{\lambda}\right)^2\left(1 - \sin\left(\frac{\pi}{4} + \theta_c\right)\right)\right]$, where n_g is group refractive index, and ν and $\delta\nu$ are the center frequency and FWHM of the optical gain spectrum, respectively. This formula was used to plot the dashed curves in fig. S6, with reasonably good correspondence to the simulation and experimental results.

β_m, η, and F_m

We used theoretical models to calculate $\beta_m = F_m/F_{tot}$, $\eta = \left(1 + \frac{\tau_s}{F_{tot}\,\tau_{nr}}\right)^{-1}$, and $F_m = \frac{3\lambda^3 Q_m}{4\pi^2 V_m}$, where Q_m was calculated for WGM in spherical cavities with a diameter L and $V_m = f_V V$ is mode volume. The fractional volume factor f_V was the fitting parameter. For plasmonic devices (assuming $F_u = 5$), we found $f_V \approx 0.006$, corresponding to a modal height of 3 to 10 nm. For photonic devices ($F_u = 1$), $f_V = 0.9$ produced the best fit. The fitting values for β_m, η, and F_m are in reasonable agreement with the experimental data considering the simple assumptions made, such as same V_m and Q_m for all modes. To determine the internal quantum efficiency η_{int} ($=\tau_{nr}/\tau_s$) of $CsPbBr_3$, we used as-made $CsPbBr_3$ microcrystals (dominantly with $L > 4\,\mu m$) in DMF solution. The samples were excited by using a picosecond frequency doubled laser (λ = 382 nm) at low pumping ($\rho_p = \sim 10^{16}\ cm^{-3}$). The total magnitude of output fluorescence was measured. This apparatus was calibrated with respect to 10 μM of fluorescein dye in 0.1 N NaOH aqueous solution (*53*), which has a known η of 0.92. The measured intrinsic η of the $CsPbBr_3$ samples was 0.015. Using time-correlated single-photon counting, fluorescence lifetime was measured. Total lifetime constant was extracted from the exponential fit to the fluorescence decay curves using $\tau_{tot} = A_1\tau_1 + A_2\tau_2$. The radiative decay time constant τ_s of the sample is related to τ_{tot} and η_{int} by using $\tau_s = \tau_{tot}\eta_{int}$.

Threshold carrier density

The density of absorbed pump photons, ρ_p, at threshold can be expressed as $\rho_p = \zeta E_{th}/(L_z\,\hbar\omega_p)$, where L_z is the height of the gain medium, $\hbar\omega_p$ ($=4 \times 10^{-19}$ J) is the energy of single pump photon, and ζ is a conversion factor related to the reflection and absorption of the pump light. The conversion factor is shown to be (*6*): $\zeta = (1 - R_1) - [R_2(1 - R_1)e^{-kLz} + (1 - R_2)](1 - R_1)e^{-kLz}/(1 - R_1R_2e^{-2kLz})$, where R_1 and R_2 are reflectivities and k is the absorption coefficient of $CsPbBr_3$ for the pump wavelength ($10^4\ cm^{-1}$ at 293 K) (*54*). For a $CsPbBr_3$ cube with a height of 1 μm, a total of 52 and 55% of the pump light is absorbed in plasmonic and photonic devices, respectively. The total absorbed pump photons can be converted to the rate of absorption of photon pumps per volume, P_{th}. In our experiments, the pump light is nanosecond pulses with a pulse duration of τ_p. Then, the time-averaged absorption rate is given by $P_{th} = \rho_p/\tau_p$. For example, for a 1-μm-high plasmonic laser device that reaches its lasing threshold at $E_{th} = 0.46\ mJ/cm^2$, we get $\rho_p = 6 \times 10^{18}\ cm^{-3}$ and $P_{th} = 1.2 \times 10^{18}\ cm^{-3}\ ns^{-1}$. Last, threshold carrier density can be estimated by using $\rho_{th} = P_{th}\tau_s\eta/F_{tot}$.

Theoretical curves in Fig. 9

The total Q-factor, Q_{tot}, of a cavity consists of radiative Q-factor, Q_{rad}, and absorptive Q-factor Q_{abs}: $1/Q_{tot} = 1/Q_{rad} + 1/Q_{abs}$. The radiative Q-factor of WGM in a spherical cavity using the analytic equation was calculated using an approximate formula (*55*). The large group index and stronger surface reflection of plasmonic modes in the device boundary makes Q_{rad} for plasmonic lasers much higher than Q_{rad} in photonic devices. On the contrary, high metallic absorption (with a coefficient of α) in plasmonic devices makes Q_{abs} in photonic devices much lower than Q_{abs} in photonic devices. In submicrometer devices, these effects approximately cancel each other: Q_{tot} in plasmonic and photonic devices are about the same, according to experiments and FEM calculations, within a factor of 2. To calculate Q_{rad}, we used the well-known WGM mode theory using a core group index of 3.8, a clad index of 1.65, and absorption coefficient $\alpha = 5800\ cm^{-1}$ for plasmonic cuboidal lasers; a core group index of 4.0, a clad index of 1.95, and absorption coefficient $\alpha = 9000\ cm^{-1}$ for plasmonic microplate lasers; a core index of 2.0, a clad index of 1, and an absorption coefficient $\alpha = 600\ cm^{-1}$ for photonic cuboidal lasers; and a core index of 1.8, a clad index of 1, and an absorption coefficient $\alpha = 600\ cm^{-1}$ for photonic microplate lasers. The absorption coefficient of photonic lasers was adapted from the measured absorption spectra of $CsPbBr_3$ microcrystals presented in fig. S11B.

SUPPLEMENTARY MATERIALS

Supplementary material for this article is available at http://advances.sciencemag.org/cgi/content/full/7/35/eabf3362/DC1

REFERENCES AND NOTES

1. B. Ellis, M. A. Mayer, G. Shambat, T. Sarmiento, J. Harris, E. E. Haller, J. Vučković, Ultralow-threshold electrically pumped quantum-dot photonic-crystal nanocavity laser. *Nat. Photonics* **5**, 297–300 (2011).
2. S. Wu, S. Buckley, J. R. Schaibley, L. Feng, J. Yan, D. G. Mandrus, F. Hatami, W. Yao, J. Vučković, A. Majumdar, X. Xu, Monolayer semiconductor nanocavity lasers with ultralow thresholds. *Nature* **520**, 69–72 (2015).
3. E. Tiguntseva, K. Koshelev, A. Furasova, P. Tonkaev, V. Mikhailovskii, E. V. Ushakova, D. G. Baranov, T. Shegai, A. A. Zakhidov, Y. Kivshar, Room-temperature lasing from mie-resonant non-plasmonic nanoparticles. *ACS Nano* **14**, 8149–8156 (2020).
4. Z. Zhang, L. Yang, V. Liu, T. Hong, K. Vahala, A. Scherer, Visible submicron microdisk lasers. *Appl. Phys. Lett.* **90**, 111119 (2007).
5. A. H. Fikouras, M. Schubert, M. Karl, J. D. Kumar, S. J. Powis, A. Di Falco, M. C. Gather, Non-obstructive intracellular nanolasers. *Nat. Commun.* **9**, 4817 (2018).
6. S. Wang, X.-Y. Wang, B. Li, H.-Z. Chen, Y.-L. Wang, L. Dai, R. F. Oulton, R.-M. Ma, Unusual scaling laws for plasmonic nanolasers beyond the diffraction limit. *Nat. Commun.* **8**, 1889 (2017).
7. M. T. Hill, Y.-S. Oei, B. Smalbrugge, Y. Zhu, T. de Vries, P. J. van Veldhoven, F. W. M. van Otten, T. J. Eijkemans, J. P. Turkiewicz, H. de Waardt, E. J. Geluk, S.-H. Kwon, Y.-H. Lee, R. Nötzel, M. K. Smit, Lasing in metallic-coated nanocavities. *Nat. Photonics* **1**, 589–594 (2007).
8. M. P. Nezhad, A. Simic, O. Bondarenko, B. Slutsky, A. Mizrahi, L. Feng, V. Lomakin, Y. Fainman, Room-temperature subwavelength metallo-dielectric lasers. *Nat. Photonics* **4**, 395–399 (2010).

9. D. J. Bergman, M. I. Stockman, Surface plasmon amplification by stimulated emission of radiation: Quantum generation of coherent surface plasmons in nanosystems. *Phys. Rev. Lett.* **90**, 27402 (2003).
10. M. A. Noginov, G. Zhu, A. M. Belgrave, R. Bakker, V. M. Shalaev, E. E. Narimanov, S. Stout, E. Herz, T. Suteewong, U. Wiesner, Demonstration of a spaser-based nanolaser. *Nature* **460**, 1110–1112 (2009).
11. X. Meng, A. V. Kildishev, K. Fujita, K. Tanaka, V. M. Shalaev, Wavelength-tunable spasing in the visible. *Nano Lett.* **13**, 4106–4112 (2013).
12. G. Kewes, K. Herrmann, R. Rodríguez-Oliveros, A. Kuhlicke, O. Benson, K. Busch, Limitations of particle-based spasers. *Phys. Rev. Lett.* **118**, 237402 (2017).
13. Z. Wang, X. Meng, A. V. Kildishev, A. Boltasseva, V. M. Shalaev, Nanolasers enabled by metallic nanoparticles: From spasers to random lasers. *Laser Photon. Rev.* **11**, 1700212 (2017).
14. A. Fernandez-Bravo, D. Wang, E. S. Barnard, A. Teitelboim, C. Tajon, J. Guan, G. C. Schatz, B. E. Cohen, E. M. Chan, P. J. Schuck, Ultralow-threshold, continuous-wave upconverting lasing from subwavelength plasmons. *Nat. Mater.* **18**, 1172–1176 (2019).
15. R. F. Oulton, V. J. Sorger, T. Zentgraf, R.-M. Ma, C. Gladden, L. Dai, G. Bartal, X. Zhang, Plasmon lasers at deep subwavelength scale. *Nature* **461**, 629–632 (2009).
16. Y.-J. Lu, J. Kim, H.-Y. Chen, C. Wu, N. Dabidian, C. E. Sanders, C.-Y. Wang, M.-Y. Lu, B.-H. Li, X. Qiu, W.-H. Chang, L.-J. Chen, G. Shvets, C.-K. Shih, S. Gwo, Plasmonic nanolaser using epitaxially grown silver film. *Science* **337**, 450–453 (2012).
17. R.-M. Ma, R. F. Oulton, V. J. Sorger, G. Bartal, X. Zhang, Room-temperature sub-diffraction-limited plasmon laser by total internal reflection. *Nat. Mater.* **10**, 110–113 (2011).
18. Q. Zhang, G. Li, X. Liu, F. Qian, Y. Li, T. C. Sum, C. M. Lieber, Q. Xiong, A room temperature low-threshold ultraviolet plasmonic nanolaser. *Nat. Commun.* **5**, 4953 (2014).
19. H. Cho, S.-H. Jeong, M.-H. Park, Y.-H. Kim, C. Wolf, C.-L. Lee, J. H. Heo, A. Sadhanala, N. Myoung, S. Yoo, Overcoming the electroluminescence efficiency limitations of perovskite light-emitting diodes. *Science* **350**, 1222–1225 (2015).
20. Y. Cao, N. Wang, H. Tian, J. Guo, Y. Wei, H. Chen, Y. Miao, W. Zou, K. Pan, Y. He, Perovskite light-emitting diodes based on spontaneously formed submicrometre-scale structures. *Nature* **562**, 249–253 (2018).
21. M. A. Green, A. Ho-Baillie, H. J. Snaith, The emergence of perovskite solar cells. *Nat. Photonics* **8**, 506–514 (2014).
22. G. R. Yettapu, D. Talukdar, S. Sarkar, A. Swarnkar, A. Nag, P. Ghosh, P. Mandal, Terahertz conductivity within colloidal $CsPbBr_3$ perovskite nanocrystals: Remarkably high carrier mobilities and large diffusion lengths. *Nano Lett.* **16**, 4838–4848 (2016).
23. P. Geiregat, J. Maes, K. Chen, E. Drijvers, J. De Roo, J. M. Hodgkiss, Z. Hens, Using bulk-like nanocrystals to probeintrinsic optical gain characteristics of inorganic lead halide perovskites. *ACS Nano* **12**, 10178–10188 (2018).
24. S. Cho, S. H. Yun, Structure and optical properties of perovskite-embedded dual-phase microcrystals synthesized by sonochemistry. *Commun. Chem.* **3**, 15 (2020).
25. S. Cho, S. H. Yun, Poly (catecholamine) coated $CsPbBr_3$ perovskite microlasers: lasing in water and biofunctionalization. *Adv. Funct. Mater.* **31**, 2101902 (2021).
26. Y. Yang, O. D. Miller, T. Christensen, J. D. Joannopoulos, M. Soljacic, Low-loss plasmonic dielectric nanoresonators. *Nano Lett.* **17**, 3238–3245 (2017).
27. T. P. H. Sidiropoulos, R. Röder, S. Geburt, O. Hess, S. A. Maier, C. Ronning, R. F. Oulton, Ultrafast plasmonic nanowire lasers near the surface plasmon frequency. *Nat. Phys.* **10**, 870–876 (2014).
28. A. W. Poon, F. Courvoisier, R. K. Chang, Multimode resonances in square-shaped optical microcavities. *Opt. Lett.* **26**, 632–634 (2001).
29. S. Wang, H.-Z. Chen, R.-M. Ma, High performance plasmonic nanolasers with external quantum efficiency exceeding 10%. *Nano Lett.* **18**, 7942–7948 (2018).
30. K. Okamoto, I. Niki, A. Shvartser, Y. Narukawa, T. Mukai, A. Scherer, Surface-plasmon-enhanced light emitters based on InGaN quantum wells. *Nat. Mater.* **3**, 601–605 (2004).
31. K. J. Russell, T.-L. Liu, S. Cui, E. L. Hu, Large spontaneous emission enhancement in plasmonic nanocavities. *Nat. Photonics* **6**, 459–462 (2012).
32. S. Cho, M. Humar, N. Martino, S. H. Yun, Laser particle stimulated emission microscopy. *Phys. Rev. Lett.* **117**, 193902 (2016).
33. I. Dursun, Y. Zheng, T. Guo, M. De Bastiani, B. Turedi, L. Sinatra, M. A. Haque, B. Sun, A. A. Zhumekenov, M. I. Saidaminov, Efficient photon recycling and radiation trapping in cesium lead halide perovskite waveguides. *ACS Energy Lett.* **3**, 1492–1498 (2018).
34. X. Yang, H. Xie, E. Alonas, Y. Liu, X. Chen, P. J. Santangelo, Q. Ren, P. Xi, D. Jin, Mirror-enhanced super-resolution microscopy. *Light Sci. Appl.* **5**, e16134 (2016).
35. E. Mudry, E. Le Moal, P. Ferrand, P. C. Chaumet, A. Sentenac, Isotropic diffraction-limited focusing using a single objective lens. *Phys. Rev. Lett.* **105**, 203903 (2010).
36. B. Wu, K. Fu, N. Yantara, G. Xing, S. Sun, T. C. Sum, N. Mathews, Charge accumulation and hysteresis in perovskite-based solar cells: An electro-optical analysis. *Adv. Energy Mater.* **5**, 1500829 (2015).
37. W. Lee, H. Li, A. B. Wong, D. Zhang, M. Lai, Y. Yu, Q. Kong, E. Lin, J. J. Urban, J. C. Grossman, Ultralow thermal conductivity in all-inorganic halide perovskites. *Proc. Natl. Acad. Sci. U.S.A.* **114**, 8693–8697 (2017).
38. A. P. Schlaus, M. S. Spencer, K. Miyata, F. Liu, X. Wang, I. Datta, M. Lipson, A. Pan, X.-Y. Zhu, How lasing happens in $CsPbBr_3$ perovskite nanowires. *Nat. Commun.* **10**, 265 (2019).
39. B. R. Sutherland, S. Hoogland, M. M. Adachi, P. Kanjanaboos, C. T. O. Wong, J. J. McDowell, J. Xu, O. Voznyy, Z. Ning, A. J. Houtepen, Perovskite thin films via atomic layer deposition. *Adv. Mater.* **27**, 53–58 (2015).
40. C. L. Davies, M. R. Filip, J. B. Patel, T. W. Crothers, C. Verdi, A. D. Wright, R. L. Milot, F. Giustino, M. B. Johnston, L. M. Herz, Bimolecular recombination in methylammonium lead triiodide perovskite is an inverse absorption process. *Nat. Commun.* **9**, 293 (2018).
41. A. Chernikov, C. Ruppert, H. M. Hill, A. F. Rigosi, T. F. Heinz, Population inversion and giant bandgap renormalization in atomically thin WS_2 layers. *Nat. Photonics* **9**, 466–470 (2015).
42. K. Miyata, D. Meggiolaro, M. T. Trinh, P. P. Joshi, E. Mosconi, S. C. Jones, F. De Angelis, X.-Y. Zhu, Large polarons in lead halide perovskites. *Sci. Adv.* **3**, e1701217 (2017).
43. T. J. S. Evans, K. Miyata, P. P. Joshi, S. Maehrlein, F. Liu, X.-Y. Zhu, Competition between hot-electron cooling and large polaron screening in $CsPbBr_3$ perovskite single crystals. *J. Phys. Chem. C* **122**, 13724–13730 (2018).
44. J. Zhang, N. Tansu, Optical gain and laser characteristics of InGaN quantum wells on ternary InGaN substrates. *IEEE Photonics J.* **5**, 2600111 (2013).
45. S.-L. Wang, S. Wang, X.-K. Man, R.-M. Ma, Loss and gain in a plasmonic nanolaser. *Nanophotonics* **9**, 3403–3408 (2020).
46. Q. Dong, Y. Fang, Y. Shao, P. Mulligan, J. Qiu, L. Cao, J. Huang, Electron-hole diffusion lengths > 175 μm in solution-grown $CH_3NH_3PbI_3$ single crystals. *Science* **347**, 967–970 (2015).
47. C. Huang, W. Sun, Y. Fan, Y. Wang, Y. Gao, N. Zhang, K. Wang, S. Liu, S. Wang, S. Xiao, Formation of lead halide perovskite based plasmonic nanolasers and nanolaser arrays by tailoring the substrate. *ACS Nano* **12**, 3865–3874 (2018).
48. V. Mylnikov, S. T. Ha, Z. Pan, V. Valuckas, R. Paniagua-Dominguez, H. V. Demir, A. I. Kuznetsov, Lasing action in single subwavelength particles supporting supercavity modes. *ACS Nano* **14**, 7338–7346 (2020).
49. C. W. Hsu, B. Zhen, A. D. Stone, J. D. Joannopoulos, M. Soljačić, Bound states in the continuum. *Nat. Rev. Mater.* **1**, 16048 (2016).
50. B. A. Koscher, J. K. Swabeck, N. D. Bronstein, A. P. Alivisatos, Essentially trap-free $CsPbBr_3$ colloidal nanocrystals by postsynthetic thiocyanate surface treatment. *J. Am. Chem. Soc.* **139**, 6566–6569 (2017).
51. S. Yang, Y. Wang, P. Liu, Y.-B. Cheng, H. J. Zhao, H. G. Yang, Functionalization of perovskite thin films with moisture-tolerant molecules. *Nat. Energy* **1**, 15016 (2016).
52. G. Nedelcu, L. Protesescu, S. Yakunin, M. I. Bodnarchuk, M. J. Grotevent, M. V. Kovalenko, Fast anion-exchange in highly luminescent nanocrystals of cesium lead halide perovskites ($CsPbX_3$, X= Cl, Br, I). *Nano Lett.* **15**, 5635–5640 (2015).
53. D. Magde, R. Wong, P. G. Seybold, Fluorescence quantum yields and their relation to lifetimes of rhodamine 6G and fluorescein in nine solvents: Improved absolute standards for quantum yields. *Photochem. Photobiol.* **75**, 327–334 (2002).
54. T. J. Whitcher, J.-X. Zhu, X. Chi, H. Hu, D. Zhao, T. C. Asmara, X. Yu, M. B. H. Breese, A. H. C. Neto, Y. M. Lam, Importance of electronic correlations and unusual excitonic effects in formamidinium lead halide perovskites. *Phys. Rev. X* **8**, 21034 (2018).
55. M. Humar, S. Hyun Yun, Intracellular microlasers. *Nat. Photonics* **9**, 572–576 (2015).
56. R. J. Elliott, Intensity of optical absorption by excitons. *Phys. Rev.* **108**, 1384–1389 (1957).
57. M. Saba, M. Cadelano, D. Marongiu, F. Chen, V. Sarritzu, N. Sestu, C. Figus, M. Aresti, R. Piras, A. G. Lehmann, Correlated electron–hole plasma in organometal perovskites. *Nat. Commun.* **5**, 5049 (2014).
58. R.-M. Ma, R. F. Oulton, Applications of nanolasers. *Nat. Nanotechnol.* **14**, 12–22 (2019).
59. S. I. Azzam, A. V. Kildishev, R.-M. Ma, C.-Z. Ning, R. Oulton, V. M. Shalaev, M. I. Stockman, J.-L. Xu, X. Zhang, Ten years of spasers and plasmonic nanolasers. *Light Sci. Appl.* **9**, 90 (2020).
60. E. K. Keshmarzi, R. N. Tait, P. Berini, Single-mode surface plasmon distributed feedback lasers. *Nanoscale* **10**, 5914–5922 (2018).
61. M. Ramezani, A. Halpin, A. I. Fernández-Domínguez, J. Feist, S. R.-K. Rodriguez, F. J. Garcia-Vidal, J. G. Rivas, Plasmon-exciton-polariton lasing. *Optica* **4**, 31–37 (2017).
62. Y.-H. Chou, Y.-M. Wu, K.-B. Hong, B.-T. Chou, J.-H. Shih, Y.-C. Chung, P.-Y. Chen, T.-R. Lin, C.-C. Lin, S.-D. Lin, High-operation-temperature plasmonic nanolasers on single-crystalline aluminum. *Nano Lett.* **16**, 3179–3186 (2016).
63. A. E. Siegman, *An Introduction to Lasers and Masers* (McGraw-Hill, 1971).
64. H. Haug, S. Schmitt-Rink, Electron theory of the optical properties of laser-excited semiconductors. *Prog. Quantum Electron.* **9**, 3–100 (1984).
65. H. Deng, G. Weihs, D. Snoke, J. Bloch, Y. Yamamoto, Polariton lasing vs. photon lasing in a semiconductor microcavity. *Proc. Natl. Acad. Sci. U.S.A.* **100**, 15318–15323 (2003).

Acknowledgments: We thank Y. Hwang for two-photon imaging, G. Li for thermal simulation, K.-H. Kim for ellipsometry measurement, and A. Liapis for graphic illustration. **Funding:** This research was supported by NIH (grant no. DP1EB024242) and the Massachusetts General Hospital Research Scholar Award. S.C. acknowledges the Samsung Scholarship and

Wellman-Bullock Fellowship. Part of this work used the facilities in the Center for Materials Science and Engineering at MIT and the Center for Nanoscale Systems (supported by NSF grant no. 1541959). This material is based on work supported, in part, by the U.S. Army Research Office through the Institute for Soldier Nanotechnologies at MIT, under collaborative agreement number W911NF-18-2-0048. This material is also based on work supported, in part, by the Air Force Office of Scientific Research under the award number FA9550-20-1-0115. **Author contributions:** S.C. and S.H.Y. designed the project. S.C. performed the experiments. Y.Y. performed FEM. S.C. and S.H.Y. analyzed the data. M.S. and S.H.Y. supervised the project. All authors contributed to manuscript writing. **Competing interests:** The authors declare that they have no competing interests. **Data and materials availability:** All data needed to evaluate the conclusions in the paper are present in the paper and/or the Supplementary Materials.

Submitted 19 October 2020
Accepted 6 July 2021
Published 25 August 2021
10.1126/sciadv.abf3362

Citation: S. Cho, Y. Yang, M. Soljačić, S. H. Yun, Submicrometer perovskite plasmonic lasers at room temperature. *Sci. Adv.* **7**, eabf3362 (2021).

Science Advances

Submicrometer perovskite plasmonic lasers at room temperature

Sangyeon Cho, Yi Yang, Marin Soljacic and Seok Hyun Yun

Sci Adv **7** (35), eabf3362.
DOI: 10.1126/sciadv.abf3362

Science Advances (ISSN 2375-2548) is published by the American Association for the Advancement of Science, 1200 New York Avenue NW, Washington, DC 20005. The title *Science Advances* is a registered trademark of AAAS.

Science Advances
AAAS

Supplementary Materials for

Submicrometer perovskite plasmonic lasers at room temperature

Sangyeon Cho, Yi Yang, Marin Soljačić, Seok Hyun Yun*

*Corresponding author. Email: syun@hms.harvard.edu

Published 25 August 2021, *Sci. Adv.* **7**, eabf3362 (2021)
DOI: 10.1126/sciadv.abf3362

This PDF file includes:

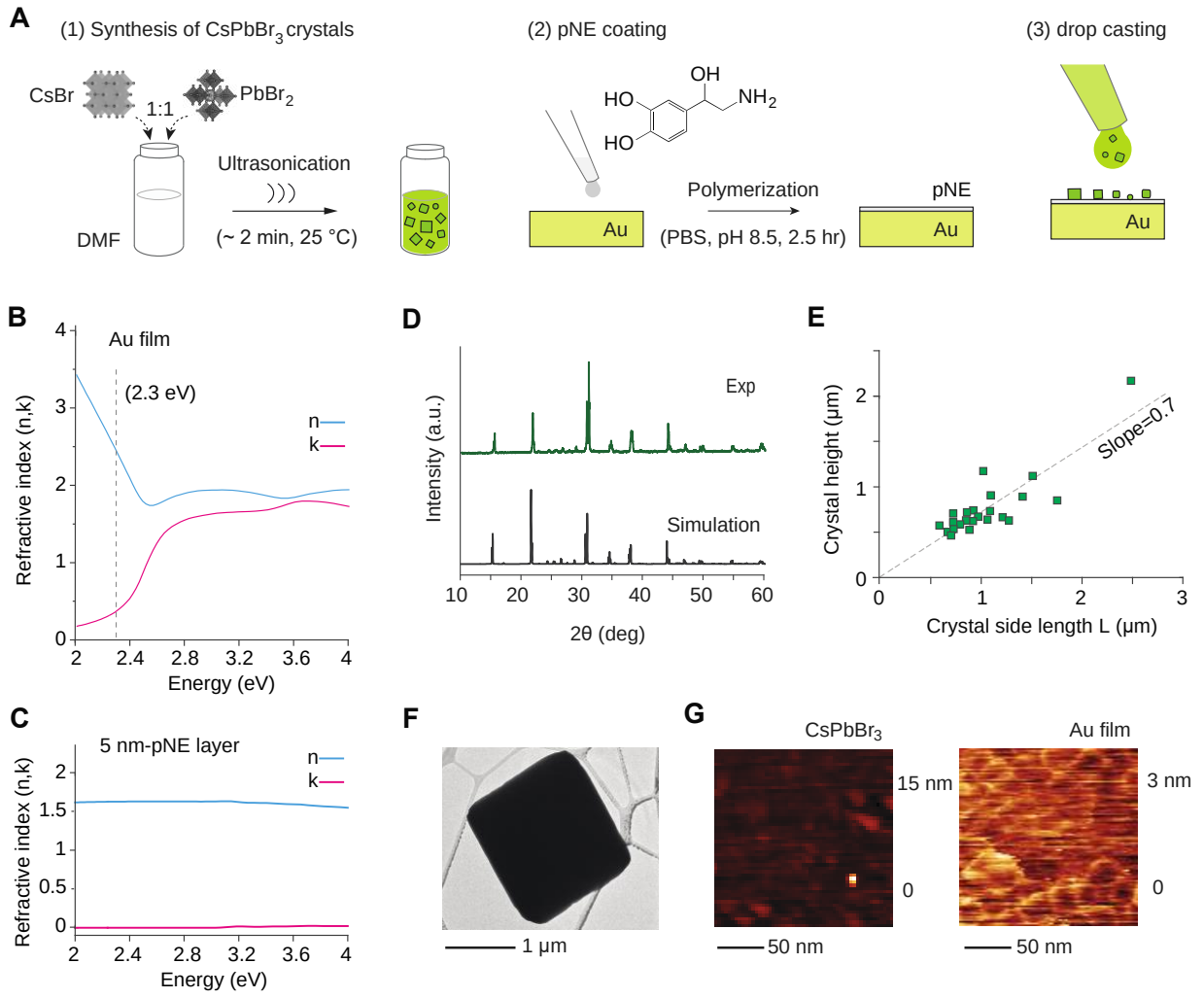

Fig. S1. Fabrication and properties of $CsPbBr_3$ crystal, pNE layer, and Au film. (A) Fabrication process. (**B-C**) Complex refractive indices (n, k) of bare Au film (**B**) and 5-nm thick pNE layer-coated on Au film (**C**) measured using spectroscopic ellipsometry. The Tauc-Lorentz dispersion model was used to fit the measured ellipsometry spectra. **(D)** Measured and simulated powder X-ray diffraction patterns assuming orthorhombic $CsPbBr_3$ (space group *Pbnm*, a = 8.20 Å, b = 8.24 Å, c = 11.74 Å). **(E)** Aspect ratios of $CsPbBr_3$ crystals measured using SEM. The linear slope of 0.7 is consistent with the orthorhombic crystal structure. **(F)** TEM image of a $CsPbBr_3$ crystal, revealing smooth surface. **(G)** AFM images of a $CsPbBr_3$ microcube and gold film, showing a root-mean-square roughness of ~ 2.1 nm for the gain crystal and ~ 0.7 nm for the gold surface.

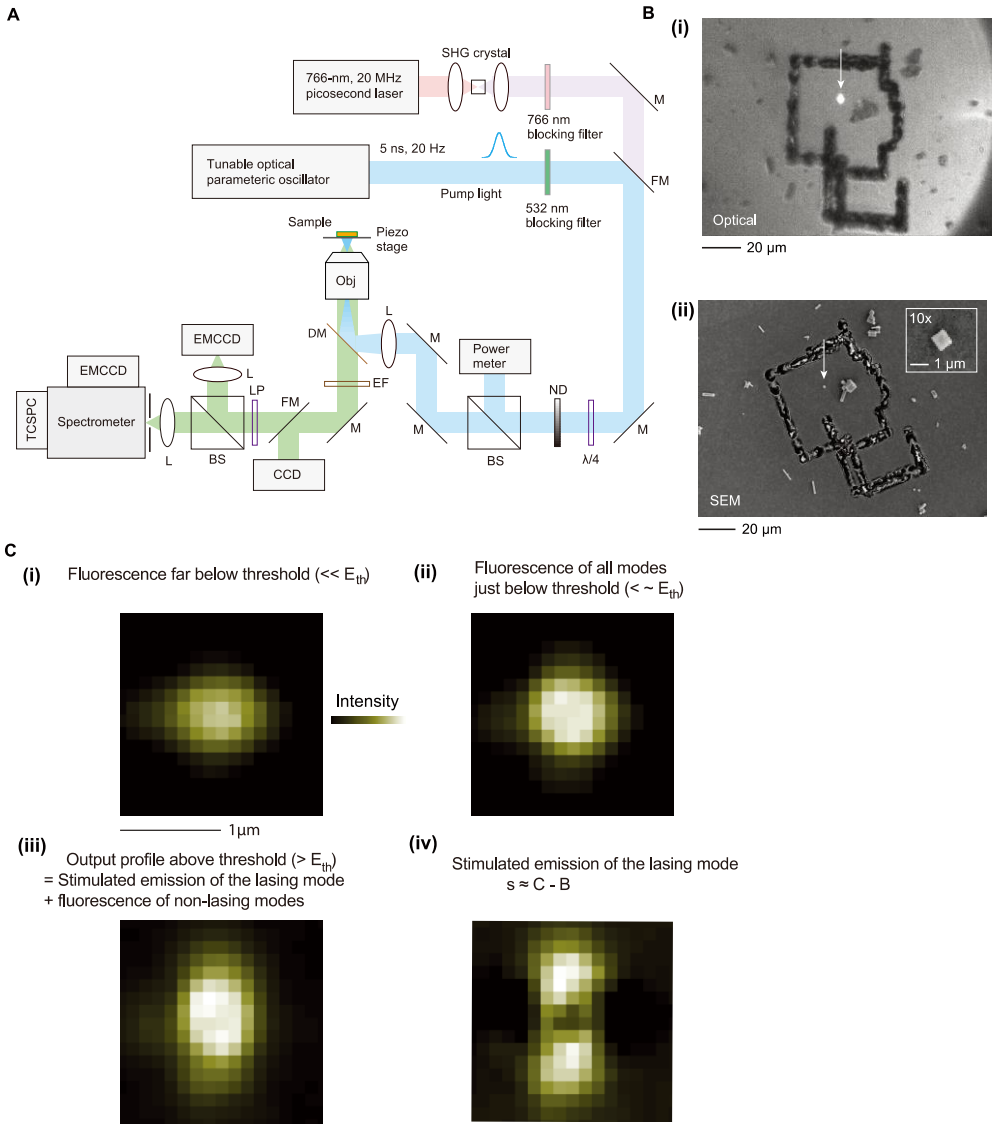

Fig. S2. Laser Characterization. (A) Schematic of the optical characterization setup. L: lens, SHG: second-harmonic generation, M: mirror, FM: flip mirror, LP: linear polarizer, DM: dichroic mirror, ND: neutral density filter, BS: beam splitter, EF: emission filter, CCD: charge-coupled device camera, EMCCD: electron-multiplication CCD camera, and TCSPC: time-correlation single-photon counter. **(B)** Marking samples for SEM. **(i)** Optical image of a laser device sample (arrow) after marking its position by deliberately creating damages on the substrate using high power laser with a specific pattern. The fluorescence from the crystal is superimposed, showing the crystal (arrow) as a bright spot. **(ii)** SEM image of the corresponding sample (arrow) identified by the particular laser damage pattern device. Inset, 10x magnified image of the $CsPbBr_3$ gain crystal. The crystal side length *L* is measured to be 0.8. **(C)** Reconstruction of the stimulated emission profile of the lasing mode. **(i)** Fluorescence image of the smallest plasmonic device *i* recorded in EMCCD at a very low pump level. **(ii)** Emission profile just below lasing threshold. **(iii)** Emission profile above threshold, which consists of the lasing mode and other non-lasing modes. **(iv)** Reconstructed emission profile of the lasing mode above threshold, obtained by subtracting **(ii)** from **(iii)**. This stimulated emission image is displayed in Fig. 3D.

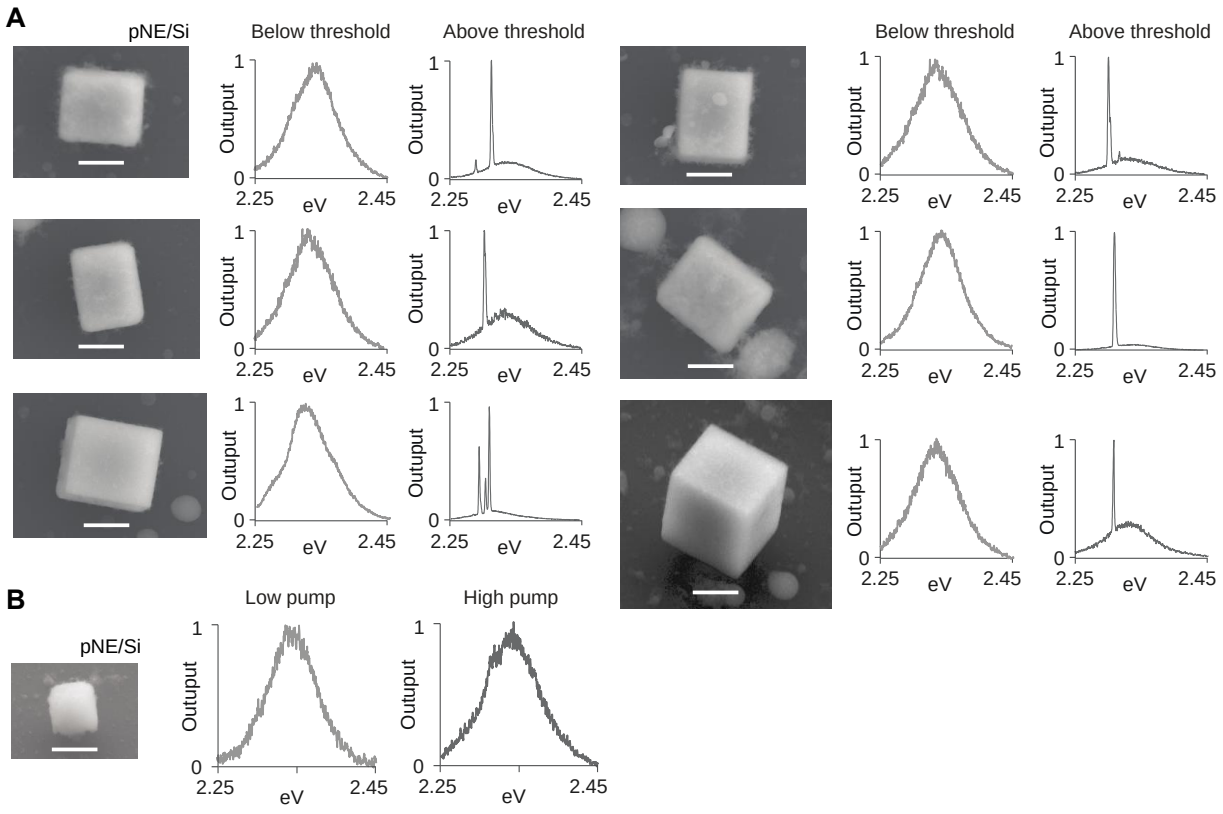

Fig. S3. Shape and spectra of photonic devices. (A) Lasing photonic micro-lasers. For each device, a representative SEM image (left), fluorescence emission (middle) below threshold (at $E = 0.2\ E_{th}$), and output spectrum (right) above lasing threshold (at $E = 1.2\ E_{th}$) are displayed. Scale bar, 1 μm. **(B)** A non-lasing submicron photonic device. An exemplary, non-lasing submicron photonic device. Mode structures are apparent in fluorescence emission spectra at both modest (< 0.5 mJ/cm^2) and high (> 2 mJ/cm^2; maximum possible without damaging the gain crystal) pump levels.

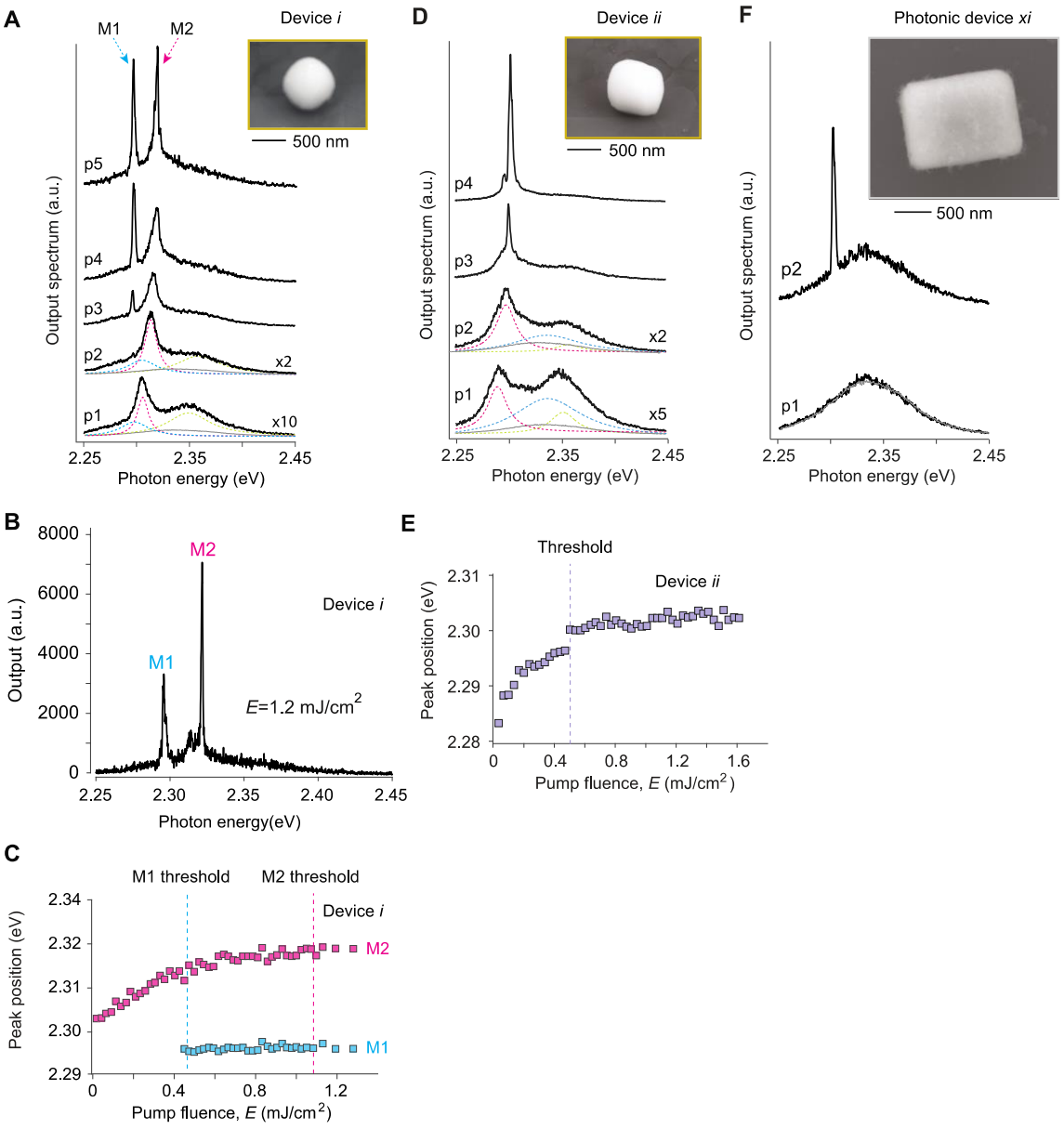

Fig. S4. Analysis of output spectra from submicron plasmonic devices. (A-C), Device *i*. **A**, PL spectra and SEM image (inset) of the smallest plasmonic laser *i* (L=0.57 μm) at various pump levels: p1 = 0.18, p2 = 0.33, p3 = 0.6, p4 = 0.88, and p5 = 1.1 mJ/cm^2. The spectra were fitted with multi-peak Lorentzian functions and typical fluorescence profile of $CsPbBr_3$. The number of Lorentzians (N) was decided using an analytical ray tracing model (See fig. S6). Two lasing modes are assigned as 'M1' (cyan curves) and 'M2' (magenta curves). Light green curve: non-lasing mode, Grey curve: typical fluorescence profile of $CsPbBr_3$. **B**, A representative output spectrum from a single pump pulse at E=1.2 mJ/cm^2 showing lasing of both modes. **C**, Spectral peak of the lasing modes (M1 and M2) as a function of pump fluence. **(D-E)**, Device *ii*. **D,** PL spectra from device *ii* (L= 0.61 μm) at various pump levels: p1 = 0.24, p2 = 0.57, p3 = 0.83, and p4 = 1.38 mJ/cm^2. **E**, Spectral peak of the mode. Dashed lines represent the threshold of the mode. **(F)** PL spectra from the photonic device *xi* (L=1.2 μm).

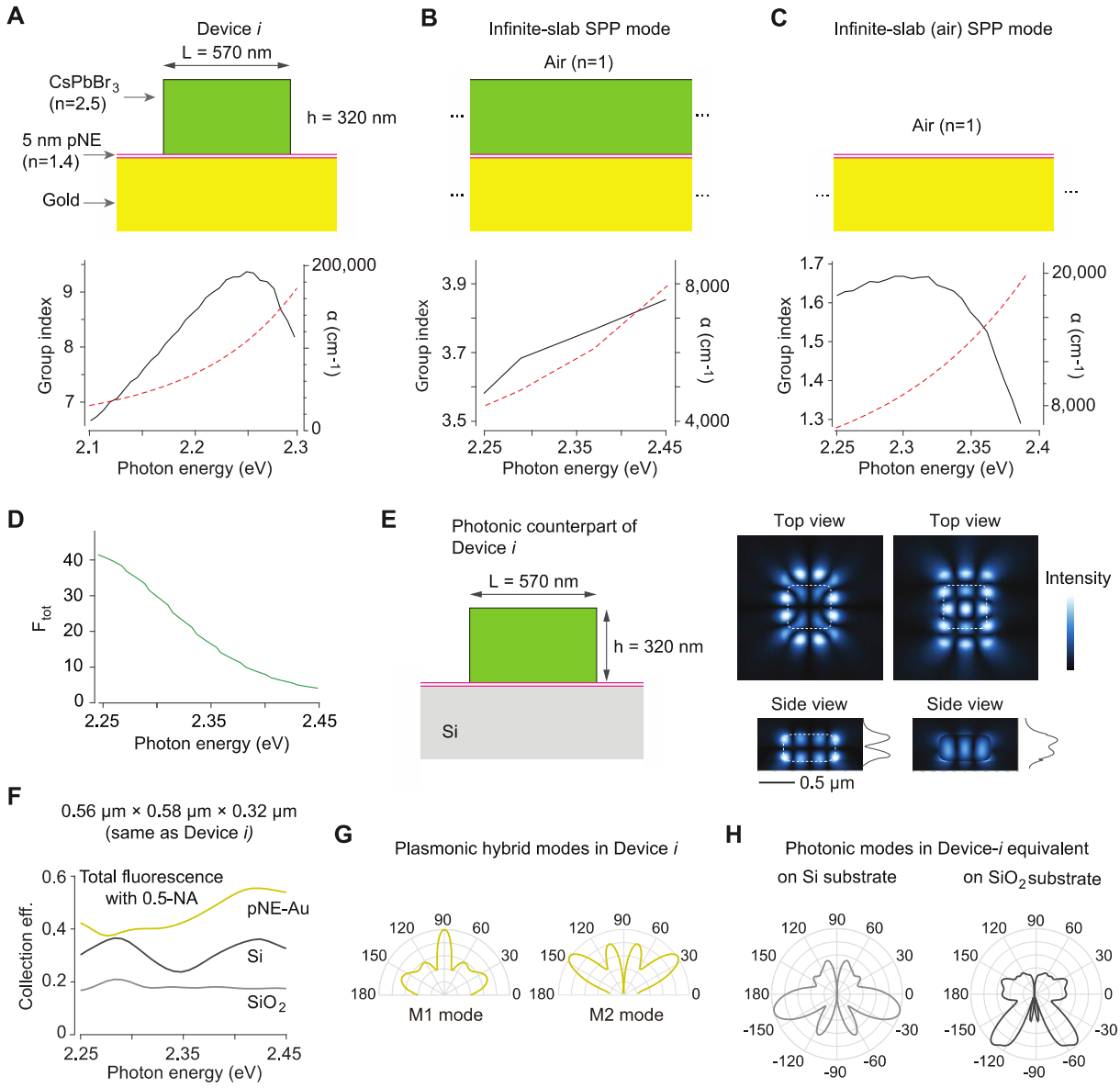

Fig. S5. FEM calculation results. (A) Dispersion of a pure-SPP mode supported in the plasmonic device *i* (Fig. 1B). **(B)** Dispersion of a SPP wave guided in the perovskite-gold interface in a model of semi-infinite perovskite-pNE-gold slab. **(C)** Dispersion of a SPP wave guided in the air-gold interface in a semi-infinite pNE-coated gold substrate. Solid lines (black): group index of the SPP waves, dashed line (red): propagation loss. **(D)** FEM simulation of radiative Purcell factor F_{tot} for a plasmonic device with L = 0.8 μm. **(E)** FEM result for a photonic laser model equivalent to the device *i* (i.e. exactly the same except that gold is replaced by Si). Two photonic modes are shown with energy at 2.34 eV and 2.28 eV, respectively. Despite the high real-part index of Si (n = 4.1 + i 0.05 at 2.3 eV), the gain medium supports WGMs propagating in the plane parallel to the perovskite-silicon interface. The Q-factors of these modes are similar to those in photonics devices on silica substrates (n = 1.46). (**F**) Full-wave simulation results for collection efficiency of fluorescence radiated from random dipoles in a $CsPbBr_3$ microcube (same size as Device *i*). The collection lens has a 0.5 numerical aperture. Three different substrates are considered: 5 nm-pNE

coated gold (yellow), silicon (dark gray) and SiO_2 (light gray) substrates. The average collection efficiency over the perovskite's gain bandwidth between 2.25 and 2.45 eV is 0.44, 0.31 and 0.2 for 5 nm-pNE coated Au, Si, and SiO_2 substrates, respectively. (**G**) Calculated angle-resolved far-field pattern of stimulated emission from the plasmonic device *I* for M1 and M2 modes. (**H**) Calculated far-field profiles of photonic devices equivalent to the device *I*, but on Si (left) and SiO_2 (right) substrates.

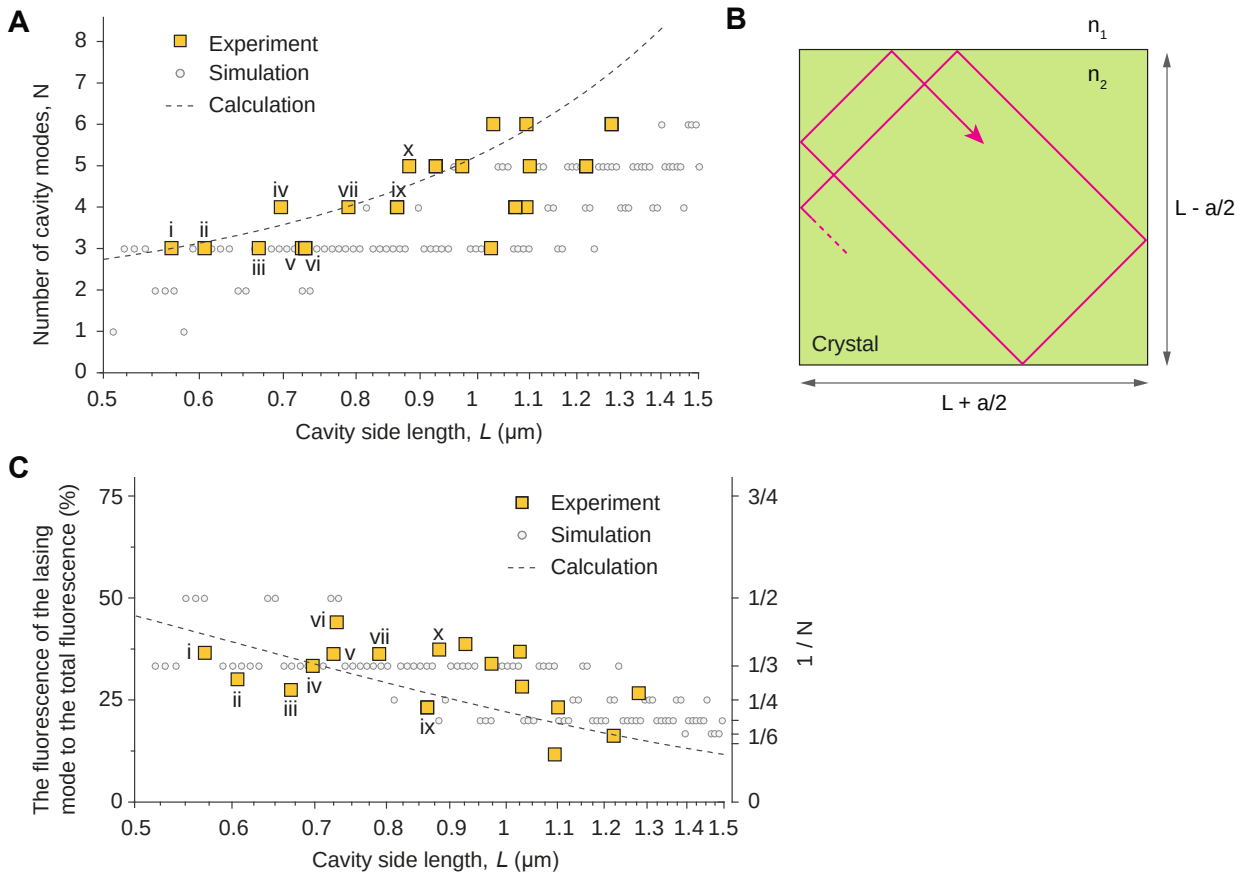

Fig. S6. Number (N) of cavity modes. (A) The number of cavity modes N in the plasmonic devices. Square: experimental data, circles: simulation result, and dashed line: analytic approximation. **(B)** Schematic of the 2D rectangular cavity model. **(C)** A plot of $1/N$. Square: the magnitude ratio of the fluorescence emission from the lasing mode (below threshold) over the total fluorescence, circles: simulation result for $1/N$, and dashed line: analytic approximation.

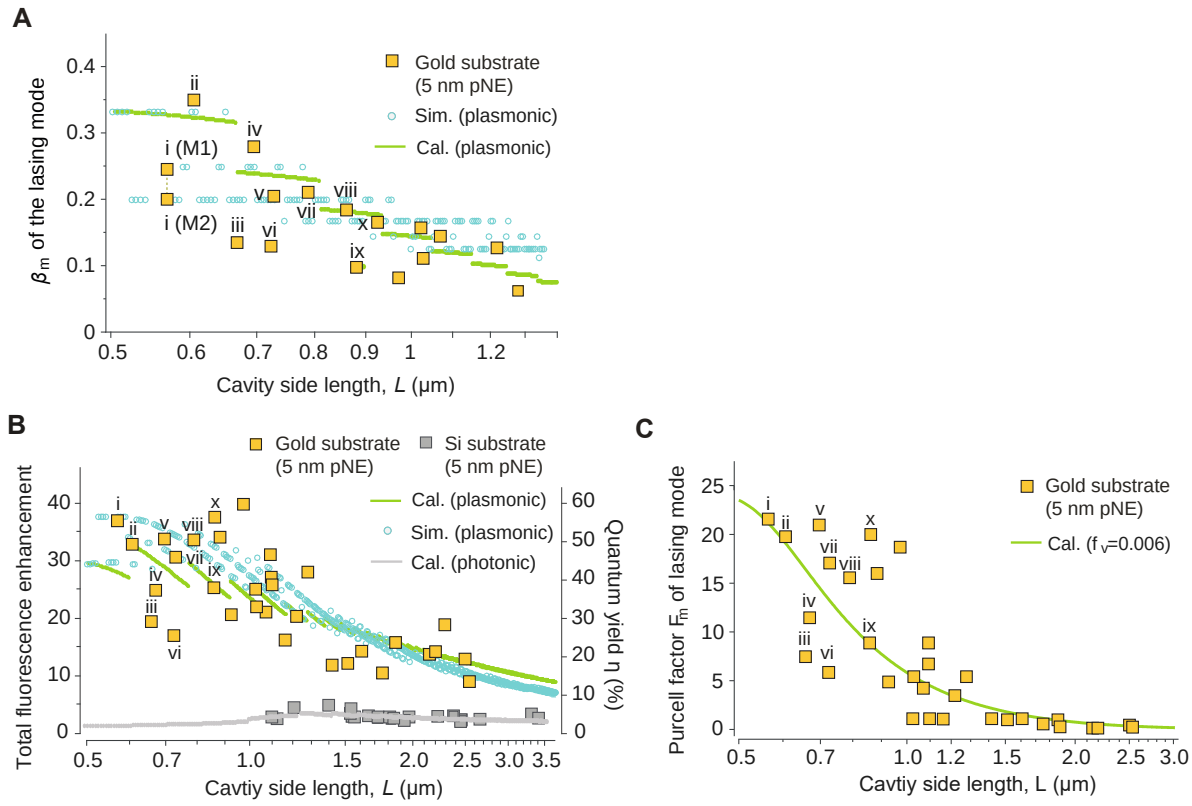

Fig. S7. Analytic model tracking the general trends of β_m, η and F_m. (A) The spontaneous emission factor of the lasing mode β_m for the plasmonic devices (yellow squares) and an analytical model (green curves) and a simulation result (cyan circles). **(B)** Fluorescence intensity measured from plasmonic (yellow) and photonic (grey) devices, and their quantum yields η estimated rom the data relative to reference, larger (> 5 μm, $\eta \approx 1.5\%$) $CsPbBr_3$ crystals on Si (data not shown). Curves: analytic calculations. Circles: simulation result. **(C)** Purcell factor of the lasing mode, F_m, of the plasmonic lasers (Squares: experimental data; curve, analytic fit).

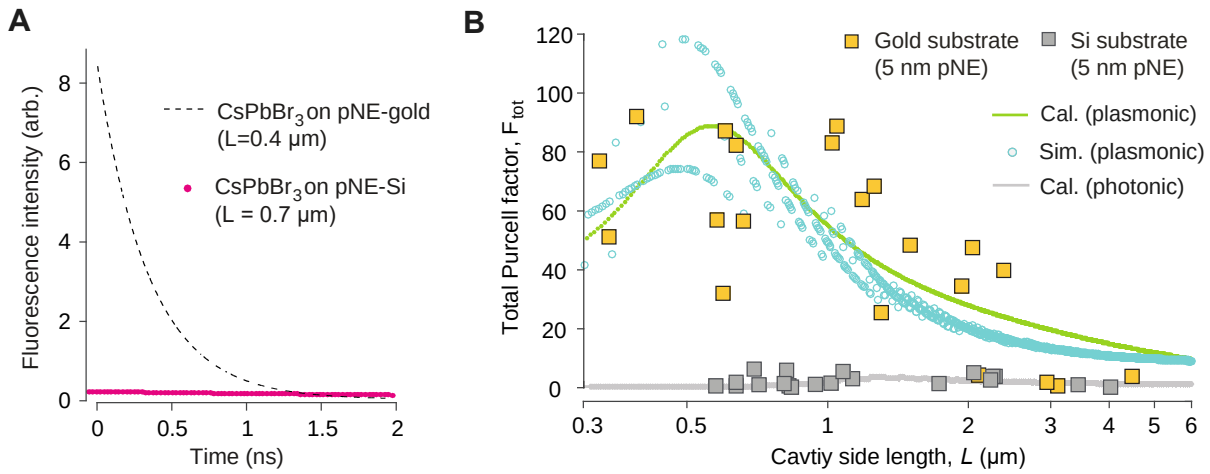

Fig. S8. Purcell factors measured by lifetime measurement. (A) Transient PL curves of photonic $CsPbBr_3$ submicron crystals on pNE-Si substrates (magenta circles) and a plasmonic crystal on pNE-gold (dashed line, Fig. 6C). **(B)** Total Purcell factor, F_{tot}, from 23 $CsPbBr_3$ samples on gold and 20 samples on Si, in reference to the mean value of large $CsPbBr_3$ crystals (dominantly $L > 5$ μm) on Si substrates. Note that lasing experiments were not performed for these samples, so some of these samples may be non-lasing even at high pump levels (> 2 mJ/cm^2). Squares: experimental data; Solid curves: analytic calculation, Circles: simulation result. Both analytic calculation and simulations were computed using f_v = 0.006 for plasmonic devices (green) and f_v = 0.9 for photonic devices (grey).

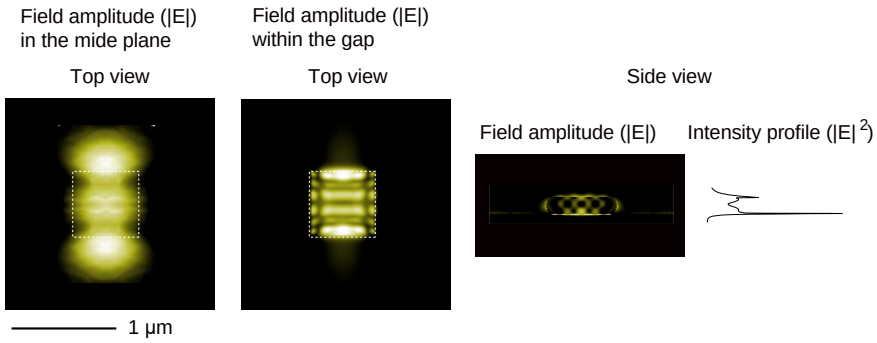

Fig. S9. FEM result of the lasing mode in device *xii*. Field amplitude (|E|) and intensity ($|E|^2$) profiles of the mode. The result shows the Fabry-Perot nature of the hybrid plasmonic mode.

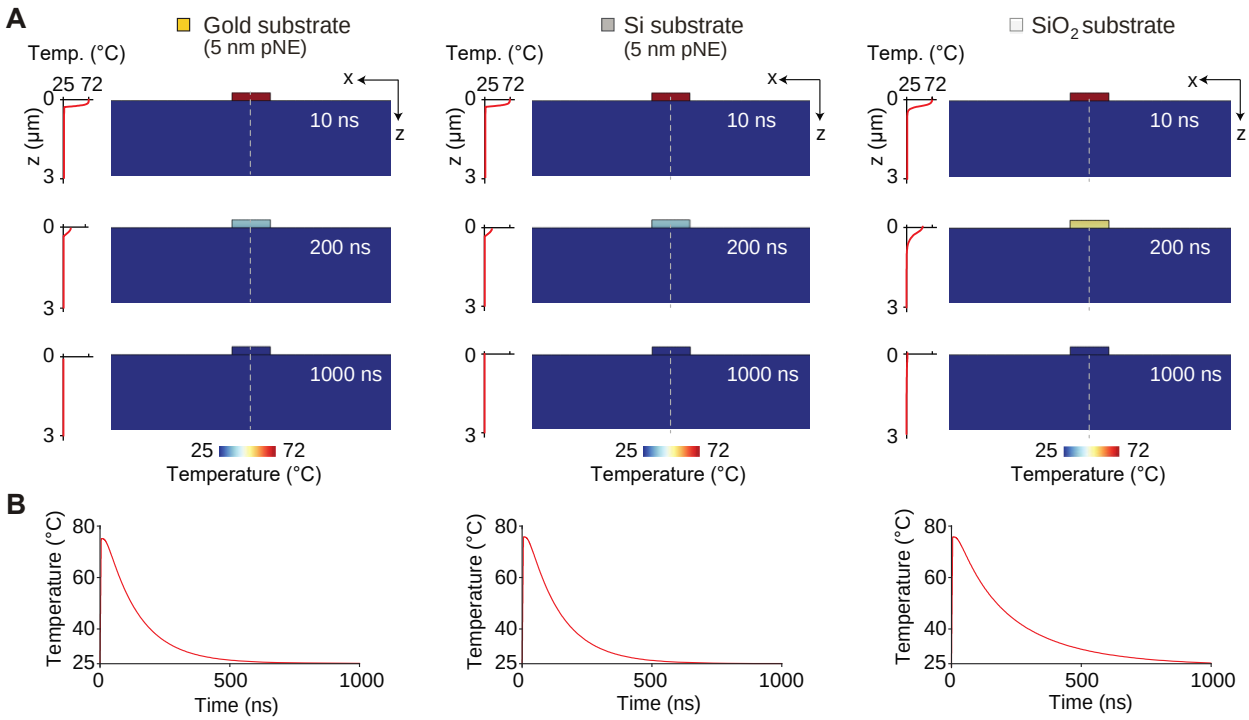

Fig. S10. Thermal stability simulations. (**A**) Time-dependent two-dimensional (x-z plane) temperature distribution for a representative $CsPbBr_3$ crystal with a size of 0.57 µm × 0.32 µm on different substrates (left: gold-coated glass, middle: silicon, right: glass). Heat source (Energy: 3 pJ, 1 mJ/cm^2) is turned on at t = 0 s for 5 ns. (**B**) Simulated transient temperature profiles in the middle of the crystal for different substrates (left: gold-coated glass, middle: silicon, right: glass).

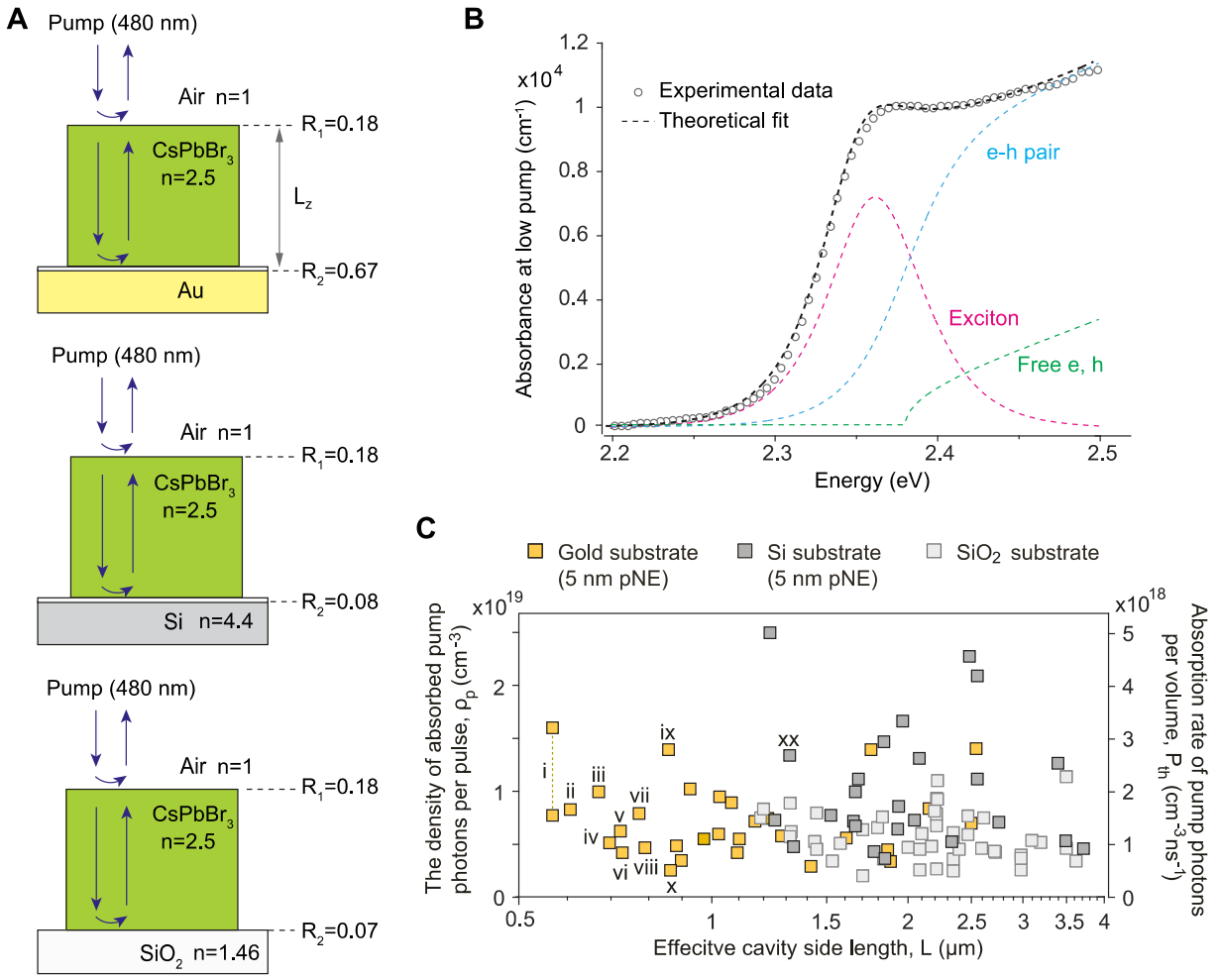

Fig. S11. Pump absorption. (A) Ray-optic illustration of the pump light paths for the cases of gold, Si, and SiO_2 substrates, respectively. The ray-optic analysis is good approximation when the size of the gain medium is > 0.5 μm, in which case the gain medium can be considered a multimode waveguide for the pump light. **(B)** Absorption spectra of $CsPbBr_3$ microcrystals. Circles, experimental data. Dashed curves: theoretical fits based on Elliot's theory (*56*) and Saha-Langmuir equation (*57*) for excitons with binding energy of 25 meV (magenta), electron-hole pairs (cyan), free electrons and holes (green), and a sum of these three components (Black) using Elliott's theory. The band gap energy is 2.38 eV. **(C)** Threshold pump absorption for the three types of lasers, computed from the experimentally measured threshold pump fluence (E_{th}) (Fig. 4A) by considering pump reflection at the substrate.

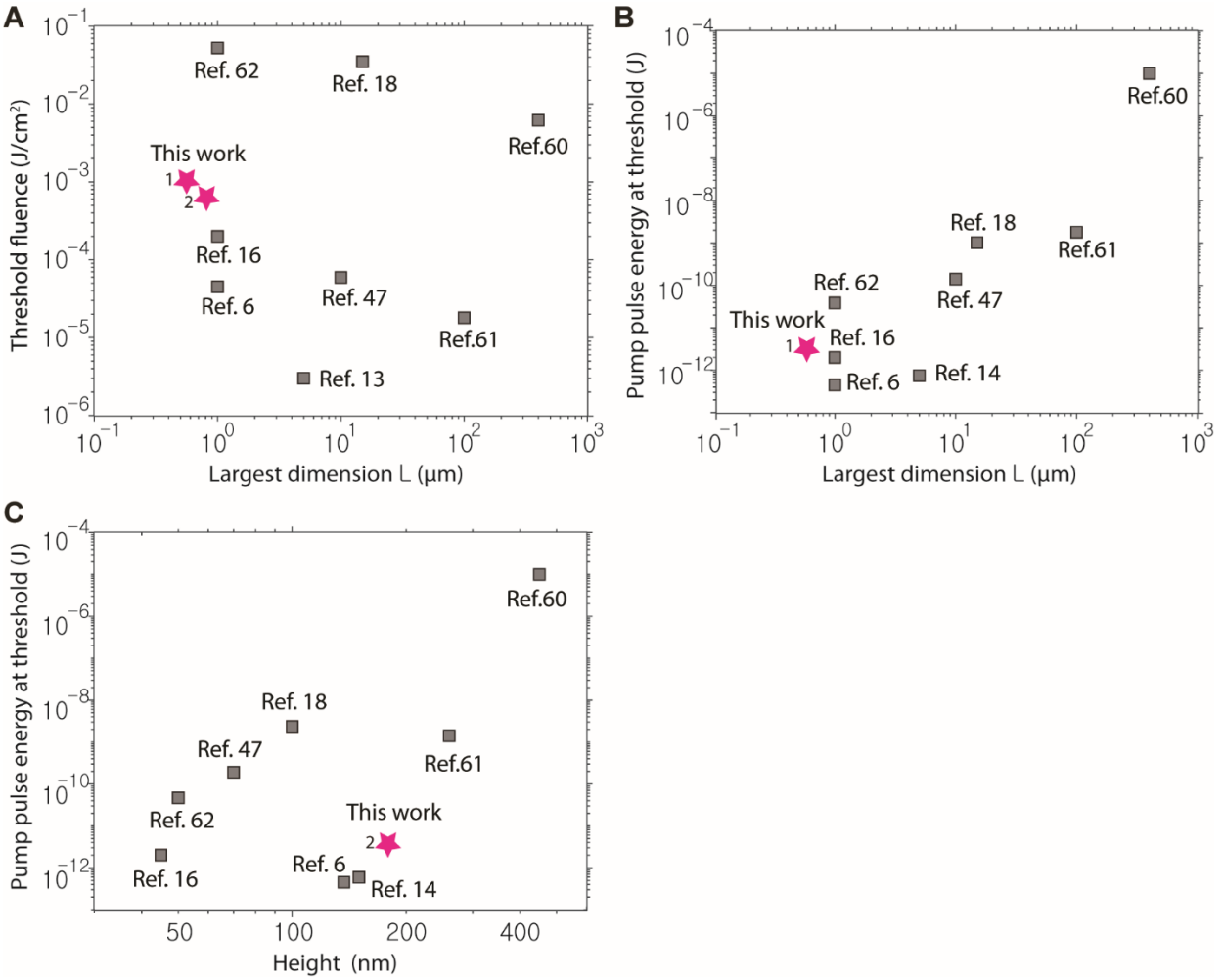

Fig. S12. Comparison of our plasmonic devices to previously reported room-temperature visible plasmonic lasers. (**A**) Threshold fluence versus side length. (**B**) Pulse energy versus side length. (**C**) Pulse energy versus height. Grey squares: previously reported data with references. Red stars: this work using $CsPbBr_3$ submicron crystals.

Table S1. A list of representative room-temperature visible plasmonic lasers demonstrated to date adopted from recent review articles (*58, 59*).

Type	Materials (wavelength)	Gain-medium size (Reported value)	Threshold (Reported value)	Pulse duration (Repetition)	Year (Ref)
Cubes	$CsPbBr_3$/Au (540 nm)	(Device 1. Length: 570 nm, Height: 320 nm Device 2. Length: 720 nm, Height: 180 nm)	(1. 1 mJ/cm^2 2. 0.7 mJ/cm^2)	5 ns (20 Hz)	This work
Nanoparticle arrays	Yb^{3+}/Er^{3+} upconversion nanoparticles/Ag (650 nm)	(Pump size: ~5 μm Height: 150 nm)	3 μJ/cm^2 (26 MW/cm^2)	120 fs (80 MHz)	2019 (*14*)
Hexagonal plates	$CH_3NH_3PbI_3$/Au (770 nm)	(Length: 10 μm Height: 50 nm)	(59.2 μJ/cm^2)	100 fs (1 kHz)	2018 (*47*)
Thin film	IR-140/Ag (810 nm)	(Length: 400 μm Height: 450 nm)	6.2 mJ/cm^2 (0.78 MW/cm^2)	8 ns (10 Hz)	2018 (*60*)
Thin film	Rylene dye/Ag (554 nm)	(Pump size: 100 μm Height: 260 nm)	(18 μJ/cm^2)	100 fs (1 kHz)	2017 (*61*)
Square Plates	CdSe/Au (700 nm)	Height: 137 nm (Length: 1 μm, Volume: 0.4 λ^3)	45 μJ/cm^2 (10 kW/cm^2)	4.5 ns (1 kHz)	2017 (*6*)
Nanowires	ZnO/Al (380 nm)	(Length: 1-4 μm Diameter: 70 nm)	53 mJ/cm^2 (105 MW/cm^2)	0.5 ns (1 kHz)	2016 (*62*)
Nanowires	GaN/Al (375 nm)	(Length: 15 μm Diameter: 100 nm)	35 mJ/cm^2 (3.5 MW/cm^2)	10 ns (100 kHz)	2014 (*18*)
Square Plates	CdS/Ag (500 nm)	(Length: 1 μm Thickness: 45 nm)	200 μJ/cm^2 (2 GW/cm^2)	100 fs (10 kHz)	2011 (*16*)

Note S1. Rate equations for a three-level laser system

A. Laser rate equation

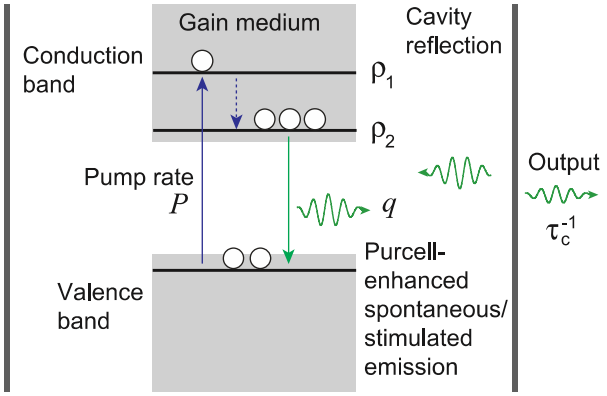

Fig. S13. Schematic of the laser model

The following rate equations can be written for a semiconductor laser (fig. S13) (*27*, *63*):

$$\frac{d}{dt}\rho_1(t) = P(t) - \frac{1}{\tau_{th}}\rho_1(t) \quad (1)$$

$$\frac{d}{dt}\rho_2(t) = \frac{1}{\tau_{th}}\rho_1(t) - \frac{\beta_m V F_{tot}}{\tau_s}[\rho_2(t) - \rho_{tr}]q(t) - \frac{F_{tot}}{\tau_s}\rho_2(t) - \frac{1}{\tau_{nr}}\rho_2(t) \quad (2)$$

$$\frac{d}{dt}q(t) = \frac{\beta_m V F_{tot}}{\tau_s}[\rho_2(t) - \rho_{tr}]q(t) + \frac{\beta F_{tot}}{\tau_s}\rho_2(t) - \frac{1}{\tau_c}q(t) \quad (3)$$

where $\rho_1(t)$ and $\rho_2(t)$ denote the carrier density in the first and second excited states, respectively, $P(t)$ is the pump rate, and τ_{th} is the rate of non-radiative thermal decay from the first to the second excited levels, ρ_{tr} is the number of carriers needed to reach transparency, $q(t)$ is the photon number density in the cavity, F_{tot} is the total enhancement factor of emission contributed by all cavity modes including non-lasing modes as well as background modes uncoupled to a cavity: i.e. F_{tot}=$\sum F_i + F_u$, where F_i is the enhancement factors of individual cavity modes and F_u is the enhancement factor for modes uncoupled to the cavity (F_u = 1 when carriers are in free space, and F_u > 1 when the emitters are interacting with plasmonic waves that have high-density of states and are non-resonant in the cavity), β_m is the spontaneous emission factor denoting the fraction of spontaneous emission into a cavity mode of interest and is related to the Purcell factor F_m of the mode ($F_m = \beta_m F_{tot}$), τ_{th} is the thermalization lifetime, τ_s is the radiative lifetime, τ_{nr} is the non-radiative lifetime, τ_c is the photon lifetime inside the cavity.

Quantum yield η is defined as the fraction of radiative emission rate over a total decay rate:

$$\eta \equiv \frac{F_{tot}/\tau_s}{F_{tot}/\tau_s + 1/\tau_{nr}} = \left(1 + \frac{\tau_s}{F_{tot}\,\tau_{nr}}\right)^{-1} \quad (4)$$

B. Lasing threshold

For pumping with a duration τ_p longer than τ_c, τ_{th}, and τ_s/F_{tot} (this condition is satisfied in our plasmonic lasers), we can set $\frac{d}{dt} = 0$ to obtain quasi-steady state solutions.:

$$P = \frac{\beta_m F_{tot} V}{\tau_s}(\rho_2 - \rho_{tr})q + \frac{F_{tot}}{\tau_s}\rho_2 + \frac{1}{\tau_{nr}}\rho_2 \qquad (5a)$$

$$0 = \frac{\beta_m F_{tot} V}{\tau_s}(\rho_2 - \rho_{tr})q + \frac{\beta F_{tot}}{\tau_s}\rho_2 - \frac{1}{\tau_c}q \qquad (5b)$$

The solution of q can be expressed, using $p \equiv P/P_{th}$, as:

$$q(p) = \tau_c P_{th} \frac{(p-1)+\sqrt{(p-1)^2+4\beta_m \eta p}}{2} \qquad (6)$$

q as a function of P has a nonlinear kink at p = 1, so this point defines a lasing threshold, and P_{th} is the pump rate at threshold.

$$P_{th}V = \frac{1}{\beta_m F_{tot}\tau_c}\left(F_{tot} + \frac{\tau_s}{\tau_{nr}}\right) + \frac{\rho_{tr}V}{\tau_s}\left(F_{tot} - \beta_m F_{tot} + \frac{\tau_s}{\tau_{nr}}\right) \qquad (7)$$

Using the quality factor of the cavity mode, $Q_m = \omega_0 \tau_c$,

$$P_{th}V = \frac{\omega_0}{\beta_m Q \eta} + \frac{F_{tot}\rho_{tr}V}{\tau_s \eta}(1 - \beta_m \eta) \qquad (8)$$

The first term describes the contribution of photon loss in the cavity, and the second term describes the required energy to reach the status of transparency or population inversion in the gain medium. For the gain material with a quantum yield near the unity (η~1),

$$P_{th}V = \frac{\omega_0}{\beta_m Q} + \frac{F_{tot}\rho_{tr}V}{\tau_s}(1 - \beta_m) \qquad (9)$$

For the gain material with a quantum yield less than unity ($\eta \ll 1$), using

$$\eta \approx \frac{F_{tot}\,\tau_{nr}}{\tau_s} \quad (10)$$

Eq. (8) can be expressed as:

$$P_{th}V \approx \frac{\omega_0}{\beta_m Q \eta} + \frac{\rho_{tr}V\tau_s}{\tau_{nr}}(1 - \beta_m \eta) \quad (11)$$

The condition that the first term is dominant over the second term can be described in terms of cavity quality factor Q, as follows:

$$Q < \frac{\tau_s \omega_0}{\beta_m F_{tot}\rho_{tr}V(1-\beta_m \eta)} \quad (12)$$

This is plotted in fig. S14 for two different cases: (1) F_{tot} = 60 and β_m = 0.1 (typical values we measured from sub-micron plasmonic lasers) and (2) F_{tot} = 20 and β_m = 0.01 (typical values we measured in micron-scale plasmonic lasers). ρ_{tr} = ~10^{18} cm^{-3} (*23*), τ_s = 250 ns, and τ_{nr} = 3.8 ns were used in both cases.

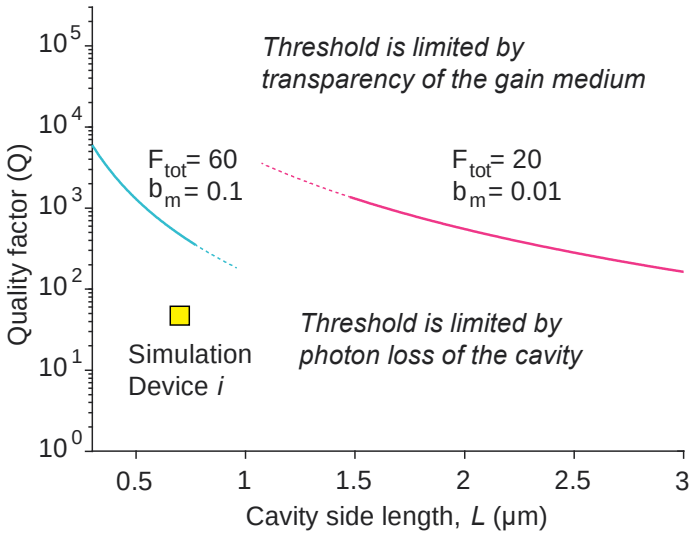

Fig. S14. The dominant contribution factor for lasing threshold. When the cavity quality factor is lower than 100, the photon loss in the cavity is the limiting factor for lasing threshold. For low-loss cavities with a quality factor much higher than 1,000, the lasing threshold is largely driven by the required energy to reach the transparency of the gain medium. Considering the metallic loss, the quality factors of our experimental plasmonic lasers are estimated to be 50-100. The quality factors of our photonic devices are < ~100 for L < 1 μm but increases with the size to $Q \approx$ 300 at L = 2 μm. Curves: a plot of Eq. (12) for two different sets of parameters. Square: finite-element simulation data for device *i*.

The second term in (11) is smaller than the first term in our plasmonic and photonic lasers. So, we can write:

$$P_{th}V \approx \frac{\omega_0}{Q_m \cdot \beta_m \cdot \eta} \qquad (13)$$

From (6) (a light-in-light-out curve), a nonlinearity parameter x can be defined as

$$x \equiv \beta_m \cdot \eta \qquad (14)$$

C. Threshold carrier density

One common definition of the lasing threshold is the point when a stimulated emission rate, $\frac{\beta_m F_{tot} V}{\tau_s}\rho_2 q$, is equal to the spontaneous emission rate, $\frac{\beta_m F_{tot}}{\tau_s}\rho_2$, into the lasing mode. This condition leads to qV = 1, which is equivalent to having one photon in the cavity mode volume. According to this definition, using Eq. (5a) we find:

$$P_{th} = \frac{\beta_m F_{tot}}{\tau_s}(\rho_{th} - \rho_{tr}) + \frac{1}{\eta}\frac{F_{tot}}{\tau_s}\rho_{th} \approx \frac{1}{\eta}\frac{F_{tot}}{\tau_s}\rho_{th} \qquad (15)$$

where ρ_{th} is the carrier density at threshold, and the approximation is valid because $\rho_{th} - \rho_{tr} < \rho_{th}/\beta_m\eta$.

From (7) and (15), we find:

$$\rho_{th}V \approx \frac{\omega_0\tau_s}{Q_m \cdot \beta_m \cdot F_{tot}} \qquad (16)$$

Another possible definition of the lasing threshold is the point when net stimulated emission rate, $\beta_m F_{avg} V(\rho_2 - \rho_{tr})/\tau_s$, is equal to the cavity loss rate, $1/\tau_c$. This condition leads to (ρ_2 at threshold is ρ_{th})

$$\rho_{th} - \rho_{tr} = \frac{\omega_0\tau_s}{Q_m \cdot \beta_m \cdot V \cdot F_{tot}} \qquad (17)$$

Since $\rho_{th} - \rho_{tr} \approx \rho_{th}$ in most cases, we find $\rho_{th}V \approx \frac{\omega_0\tau_s}{Q_m \cdot \beta_m \cdot F_{tot}}$, which is consistent with (16).

D. Transient fluorescence decay profiles

Consider fluorescence measurement using ultrashort pump pulses with a duration of τ_p. At low pump fluence below lasing threshold, the stimulated emission term in (2) is neglible. Following the absorption of a single pump pulse at t=0, the carrier density and magnitude of fluorescence decay over time:

$$\rho_2(t) = P\tau_p e^{-(\frac{F_{tot}}{\tau_s} + \frac{1}{\tau_{nr}})t} \qquad (18)$$

$$\frac{d}{dt}q(t) = \frac{F_{tot}}{\tau_s}\rho_2 = P\tau_p \frac{F_{tot}}{\tau_s} e^{-\frac{t}{\tau_{tot}}} \qquad (19)$$

where $\tau_{tot} = (\frac{F_{tot}}{\tau_s} + \frac{1}{\tau_{nr}})^{-1}$ is total decay lifetime. Integrating (19) over time yields.

$$q(t) = P\tau_p\tau_{tot}\frac{F_{tot}}{\tau_s}\left(1 - e^{-\frac{t}{\tau_{tot}}}\right) \qquad (20)$$

The total number of fluorescence photons collected is given by

$$q(\infty) = \eta \cdot P\tau_p \qquad (21)$$

where $\eta = (1 + \frac{\tau_s}{F_{tot}\,\tau_{nr}})^{-1}$ was used. For given pump pulse parameters, the total number of fluorescence photons is proportional to η, as expected from the definition of η.

From (18) we find

$$\frac{d}{dt}q(t)|_{t=0}| = F_{tot}P\tau_p/\tau_s \qquad (22)$$

For given pump pulses and intrinsic radiative time constant, the initial fluorescence peak is proportional to F_{tot}.

Note S2. Critical carrier density for the Mott transition to electron hole plasma (EHP)

At a very low carrier density, electrons and holes in $CsPbBr_3$ are strongly correlated via Coulomb interaction (*57*). As the carrier density increases, the mean distance between them decreases, and when it is less than a critical distance, electromagnetic screening become so significant that the Coulomb interaction becomes negligible. In this electron-hole plasma (EHP) state, the active carriers behave like free charges without Coulomb interaction. The phase transition to EHP is called the Mott transition. Let the critical transition density ρ_{Mott}. A model developed by Haug and Schmitt-Rink(*64*), estimates $\rho_{Mott} \approx 0.028(k_B T_e/(E_X {a_B}^3)$. Here, k_B is Boltzmann constant, T_e (= 709 K; fig. S15) is electronic temperature, a_B is Bohr radius — $a_B = a_H \varepsilon_r^X m_e/\mu \approx 3.5$ nm for $CsPbBr_3$, where a_H = 0.053 nm, μ (= 0.125) is the reduced mass of electron-hole pair(*22*), m_e is electron mass, and $\varepsilon_r^X = \sqrt{(13.6\ eV/E_X)\mu/m_e}$ is the dielectric function of Coulomb-correlated carriers — and $E_X \approx 25$ meV is exciton binding energy for $CsPbBr_3$. We find $\rho_{Mott} \approx 9\times10^{17}$ cm^{-3} for $CsPbBr_3$. In experiments, the carrier density at lasing threshold exceeds 10^{18} cm^{-3} at which the EHP state is established.

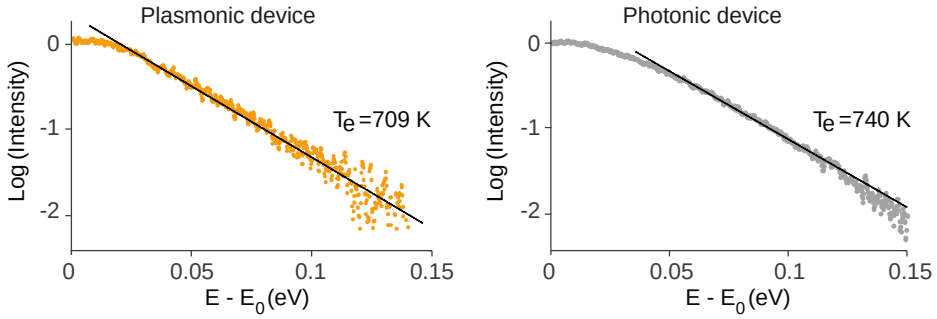

Fig. S15. Measurement of T_e for the calculation of ρ_{Mott}. The blue-wing tail of PL spectra at P =0.9 P_{th} is shown for a plasmonic (left) and a photonic (right) device. The fitting curve was the classical Maxwell-Boltzmann distribution function, which describes the EHP state(*65*): $N(E) \propto \exp(-(E-E_0)/k_B T_e)$, where $N(E)$ ($\propto I$) is the number density of carriers with energy E and E_0 is the electronic state energy at the peak PL, and T_e is electronic temperature. We found T_e to be 709 and 740 K, respectively.

Note S3. Large net gain of $CsPbBr_3$ above the Mott density

Above the Mott density (~10^{18} cm^{-3}), pump energy is absorbed in the Coulomb-correlated band structure, but all generated excitons are readily dissociated into free-charge carriers to form a hot EHP state (*57*). In this state, the band edge becomes red-shifted below the exciton peak's energy, and the absorption line follows the classical square-root dependence in direct semiconductors (*40*, *57*). This phenomenon is called bandgap renormalization (BGR). Population inversion can be built

up due to the absence of additional absorption or scattering channels (*41*). Generated hot carriers are cooled to form a cold EHP state via longitudinal optical phonon-lattice thermalization with a time scale of 0.2 ps (*23*), faster than a polaron formation time of 0.7 ps (*42*, *43*). It is noteworthy that the pumping wavelength matched to the exciton peak, so-called resonant pumping, achieved two-fold higher optical gain compared to non-resonant pumping by bypassing the phonon bottleneck (*23*). After forming the cold EHP state, the free charge carriers are recombined via stimulated emission coupled with EHP plasmon emission (i.e., collective oscillations of EHP) (*38*). Coupling to plasmon resonance changes the two-level EHP state to quasi-three level states, enabling population inversion and achieving sub-bandgap lasing (*38*). The bimolecular recombination in the EHP state is about ten times slower than the recombination below the Mott density due to the absence of Coulomb correlation ($k_B = 6.3 \times 10^{-11}$ cm^3/s) (*40*). However, owing to Purcell enhancement, the recombination could be accelerated up to 50 times, resulting in an increased optical gain. At a typical carrier density ρ_{th} of ~$10^{18}/cm^3$ for $F_p = 50$ in $CsPbBr_3$ and L = 0.6 μm, the Purcell-enhanced spontaneous emission is estimated to be 317 ps, slow enough to build up population inversion.

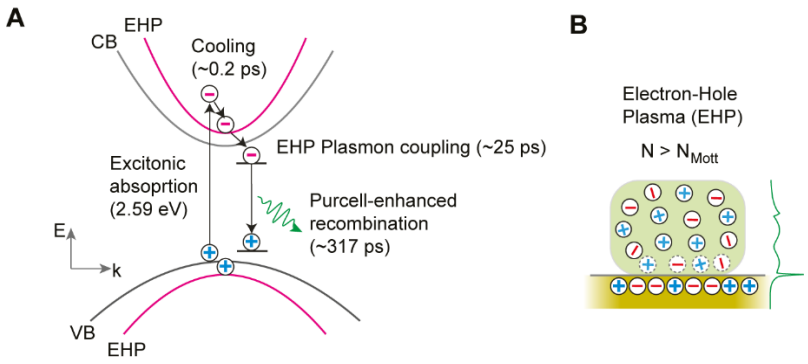

Fig. S16. Purcell-enhanced EHP lasing in $CsPbBr_3$ devices. (**A**) Illustration of plasmonic lasing process of quasi-three level of $CsPbBr_3$. (**B**) Schematic of the electron–hole plasma (EHP) state above the Mott density.

REFERENCES AND NOTES

1. B. Ellis, M. A. Mayer, G. Shambat, T. Sarmiento, J. Harris, E. E. Haller, J. Vučković, Ultralow-threshold electrically pumped quantum-dot photonic-crystal nanocavity laser. *Nat. Photonics* **5**, 297–300 (2011).
2. S. Wu, S. Buckley, J. R. Schaibley, L. Feng, J. Yan, D. G. Mandrus, F. Hatami, W. Yao, J. Vučković, A. Majumdar, X. Xu, Monolayer semiconductor nanocavity lasers with ultralow thresholds. *Nature* **520**, 69–72 (2015).
3. E. Tiguntseva, K. Koshelev, A. Furasova, P. Tonkaev, V. Mikhailovskii, E. V Ushakova, D. G. Baranov, T. Shegai, A. A. Zakhidov, Y. Kivshar, Room-temperature lasing from mie-resonant non-plasmonic nanoparticles. *ACS Nano* **14**, 8149–8156 (2020).
4. Z. Zhang, L. Yang, V. Liu, T. Hong, K. Vahala, A. Scherer, Visible submicron microdisk lasers. *Appl. Phys. Lett.* **90**, 111119 (2007).
5. A. H. Fikouras, M. Schubert, M. Karl, J. D. Kumar, S. J. Powis, A. Di Falco, M. C. Gather, Non-obstructive intracellular nanolasers. *Nat. Commun.* **9**, 4817 (2018).
6. S. Wang, X.-Y. Wang, B. Li, H.-Z. Chen, Y.-L. Wang, L. Dai, R. F. Oulton, R.-M. Ma, Unusual scaling laws for plasmonic nanolasers beyond the diffraction limit. *Nat. Commun.* **8**, 1889 (2017).
7. M. T. Hill, Y.-S. Oei, B. Smalbrugge, Y. Zhu, T. de Vries, P. J. van Veldhoven, F. W. M. van Otten, T. J. Eijkemans, J. P. Turkiewicz, H. de Waardt, E. J. Geluk, S.-H. Kwon, Y.-H. Lee, R. Nötzel, M. K. Smit, Lasing in metallic-coated nanocavities. *Nat. Photonics* **1**, 589–594 (2007).
8. M. P. Nezhad, A. Simic, O. Bondarenko, B. Slutsky, A. Mizrahi, L. Feng, V. Lomakin, Y. Fainman, Room-temperature subwavelength metallo-dielectric lasers. *Nat. Photonics* **4**, 395–399 (2010).
9. D. J. Bergman, M. I. Stockman, Surface plasmon amplification by stimulated emission of radiation: Quantum generation of coherent surface plasmons in nanosystems. *Phys. Rev. Lett.* **90**, 27402 (2003).
10. M. A. Noginov, G. Zhu, A. M. Belgrave, R. Bakker, V. M. Shalaev, E. E. Narimanov, S. Stout, E. Herz, T. Suteewong, U. Wiesner, Demonstration of a spaser-based nanolaser. *Nature* **460**, 1110–1112 (2009).
11. X. Meng, A. V Kildishev, K. Fujita, K. Tanaka, V. M. Shalaev, Wavelength-tunable spasing in the visible. *Nano Lett.* **13**, 4106–4112 (2013).
12. G. Kewes, K. Herrmann, R. Rodríguez-Oliveros, A. Kuhlicke, O. Benson, K. Busch, Limitations of particle-based spasers. *Phys. Rev. Lett.* **118**, 237402 (2017).

13. Z. Wang, X. Meng, A. V Kildishev, A. Boltasseva, V. M. Shalaev, Nanolasers enabled by metallic nanoparticles: From spasers to random lasers. *Laser Photon. Rev.* **11**, 1700212 (2017).
14. A. Fernandez-Bravo, D. Wang, E. S. Barnard, A. Teitelboim, C. Tajon, J. Guan, G. C. Schatz, B. E. Cohen, E. M. Chan, P. J. Schuck, Ultralow-threshold, continuous-wave upconverting lasing from subwavelength plasmons. *Nat. Mater.* **18**, 1172–1176 (2019).
15. R. F. Oulton, V. J. Sorger, T. Zentgraf, R.-M. Ma, C. Gladden, L. Dai, G. Bartal, X. Zhang, Plasmon lasers at deep subwavelength scale. *Nature* **461**, 629–632 (2009).
16. Y.-J. Lu, J. Kim, H.-Y. Chen, C. Wu, N. Dabidian, C. E. Sanders, C.-Y. Wang, M.-Y. Lu, B.-H. Li, X. Qiu, W.-H. Chang, L.-J. Chen, G. Shvets, C.-K. Shih, S. Gwo, Plasmonic nanolaser using epitaxially grown silver film. *Science* **337**, 450–453 (2012).
17. R.-M. Ma, R. F. Oulton, V. J. Sorger, G. Bartal, X. Zhang, Room-temperature sub-diffraction-limited plasmon laser by total internal reflection. *Nat. Mater.* **10**, 110–113 (2011).
18. Q. Zhang, G. Li, X. Liu, F. Qian, Y. Li, T. C. Sum, C. M. Lieber, Q. Xiong, A room temperature low-threshold ultraviolet plasmonic nanolaser. *Nat. Commun.* **5**, 4953 (2014).
19. H. Cho, S.-H. Jeong, M.-H. Park, Y.-H. Kim, C. Wolf, C.-L. Lee, J. H. Heo, A. Sadhanala, N. Myoung, S. Yoo, Overcoming the electroluminescence efficiency limitations of perovskite light-emitting diodes. *Science* **350**, 1222–1225 (2015).
20. Y. Cao, N. Wang, H. Tian, J. Guo, Y. Wei, H. Chen, Y. Miao, W. Zou, K. Pan, Y. He, Perovskite light-emitting diodes based on spontaneously formed submicrometre-scale structures. *Nature* **562**, 249–253 (2018).
21. M. A. Green, A. Ho-Baillie, H. J. Snaith, The emergence of perovskite solar cells. *Nat. Photonics* **8**, 506–514 (2014).
22. G. R. Yettapu, D. Talukdar, S. Sarkar, A. Swarnkar, A. Nag, P. Ghosh, P. Mandal, Terahertz conductivity within colloidal $CsPbBr_3$ perovskite nanocrystals: Remarkably high carrier mobilities and large diffusion lengths. *Nano Lett.* **16**, 4838–4848 (2016).
23. P. Geiregat, J. Maes, K. Chen, E. Drijvers, J. De Roo, J. M. Hodgkiss, Z. Hens, Using bulk-like nanocrystals to probeintrinsic optical gain characteristics of inorganic lead halide perovskites. *ACS Nano* **12**, 10178–10188 (2018).
24. S. Cho, S. H. Yun, Structure and optical properties of perovskite-embedded dual-phase microcrystals synthesized by sonochemistry. *Commun. Chem.* **3**, 15 (2020).

25. S. Cho, S. H. Yun, Poly (catecholamine) coated $CsPbBr_3$ perovskite microlasers: lasing in water and biofunctionalization. *Adv. Funct. Mater.* **31**, 2101902 (2021).
26. Y. Yang, O. D. Miller, T. Christensen, J. D. Joannopoulos, M. Soljacic, Low-loss plasmonic dielectric nanoresonators. *Nano Lett.* **17**, 3238–3245 (2017).
27. T. P. H. Sidiropoulos, R. Röder, S. Geburt, O. Hess, S. A. Maier, C. Ronning, R. F. Oulton, Ultrafast plasmonic nanowire lasers near the surface plasmon frequency. *Nat. Phys.* **10**, 870–876 (2014).
28. A. W. Poon, F. Courvoisier, R. K. Chang, Multimode resonances in square-shaped optical microcavities. *Opt. Lett.* **26**, 632–634 (2001).
29. S. Wang, H.-Z. Chen, R.-M. Ma, High performance plasmonic nanolasers with external quantum efficiency exceeding 10%. *Nano Lett.* **18**, 7942–7948 (2018).
30. K. Okamoto, I. Niki, A. Shvartser, Y. Narukawa, T. Mukai, A. Scherer, Surface-plasmon-enhanced light emitters based on InGaN quantum wells. *Nat. Mater.* **3**, 601–605 (2004).
31. K. J. Russell, T.-L. Liu, S. Cui, E. L. Hu, Large spontaneous emission enhancement in plasmonic nanocavities. *Nat. Photonics* **6**, 459–462 (2012).
32. S. Cho, M. Humar, N. Martino, S. H. Yun, Laser particle stimulated emission microscopy. *Phys. Rev. Lett.* **117**, 193902 (2016).
33. I. Dursun, Y. Zheng, T. Guo, M. De Bastiani, B. Turedi, L. Sinatra, M. A. Haque, B. Sun, A. A. Zhumekenov, M. I. Saidaminov, Efficient photon recycling and radiation trapping in cesium lead halide perovskite waveguides. *ACS Energy Lett.* **3**, 1492–1498 (2018).
34. X. Yang, H. Xie, E. Alonas, Y. Liu, X. Chen, P. J. Santangelo, Q. Ren, P. Xi, D. Jin, Mirror-enhanced super-resolution microscopy. *Light Sci. Appl.* **5**, e16134 (2016).
35. E. Mudry, E. Le Moal, P. Ferrand, P. C. Chaumet, A. Sentenac, Isotropic diffraction-limited focusing using a single objective lens. *Phys. Rev. Lett.* **105**, 203903 (2010).
36. B. Wu, K. Fu, N. Yantara, G. Xing, S. Sun, T. C. Sum, N. Mathews, Charge accumulation and hysteresis in perovskite-based solar cells: An electro-optical analysis. *Adv. Energy Mater.* **5**, 1500829 (2015).
37. W. Lee, H. Li, A. B. Wong, D. Zhang, M. Lai, Y. Yu, Q. Kong, E. Lin, J. J. Urban, J. C. Grossman, Ultralow thermal conductivity in all-inorganic halide perovskites. *Proc. Natl. Acad. Sci. U.S.A.* **114**, 8693–8697 (2017).
38. A. P. Schlaus, M. S. Spencer, K. Miyata, F. Liu, X. Wang, I. Datta, M. Lipson, A. Pan, X.-Y. Zhu, How lasing happens in $CsPbBr_3$ perovskite nanowires. *Nat. Commun.* **10**, 265 (2019).

39. B. R. Sutherland, S. Hoogland, M. M. Adachi, P. Kanjanaboos, C. T. O. Wong, J. J. McDowell, J. Xu, O. Voznyy, Z. Ning, A. J. Houtepen, Perovskite thin films via atomic layer deposition. *Adv. Mater.* **27**, 53–58 (2015).
40. C. L. Davies, M. R. Filip, J. B. Patel, T. W. Crothers, C. Verdi, A. D. Wright, R. L. Milot, F. Giustino, M. B. Johnston, L. M. Herz, Bimolecular recombination in methylammonium lead triiodide perovskite is an inverse absorption process. *Nat. Commun.* **9**, 293 (2018).
41. A. Chernikov, C. Ruppert, H. M. Hill, A. F. Rigosi, T. F. Heinz, Population inversion and giant bandgap renormalization in atomically thin WS_2 layers. *Nat. Photonics* **9**, 466–470 (2015).
42. K. Miyata, D. Meggiolaro, M. T. Trinh, P. P. Joshi, E. Mosconi, S. C. Jones, F. De Angelis, X.-Y. Zhu, Large polarons in lead halide perovskites. *Sci. Adv.* **3**, e1701217 (2017).
43. T. J. S. Evans, K. Miyata, P. P. Joshi, S. Maehrlein, F. Liu, X.-Y. Zhu, Competition between hot-electron cooling and large polaron screening in $CsPbBr_3$ perovskite single crystals. *J. Phys. Chem. C* **122**, 13724–13730 (2018).
44. J. Zhang, N. Tansu, Optical gain and laser characteristics of InGaN quantum wells on ternary InGaN substrates. *IEEE Photonics J.* **5**, 2600111 (2013).
45. S.-L. Wang, S. Wang, X.-K. Man, R.-M. Ma, Loss and gain in a plasmonic nanolaser. *Nanophotonics* **9**, 3403–3408 (2020).
46. Q. Dong, Y. Fang, Y. Shao, P. Mulligan, J. Qiu, L. Cao, J. Huang, Electron-hole diffusion lengths > 175 μm in solution-grown $CH_3NH_3PbI_3$ single crystals. *Science* **347**, 967–970 (2015).
47. C. Huang, W. Sun, Y. Fan, Y. Wang, Y. Gao, N. Zhang, K. Wang, S. Liu, S. Wang, S. Xiao, Formation of lead halide perovskite based plasmonic nanolasers and nanolaser arrays by tailoring the substrate. *ACS Nano* **12**, 3865–3874 (2018).
48. V. Mylnikov, S. T. Ha, Z. Pan, V. Valuckas, R. Paniagua-Dominguez, H. V. Demir, A. I. Kuznetsov, Lasing action in single subwavelength particles supporting supercavity modes. *ACS Nano* **14**, 7338–7346 (2020).
49. C. W. Hsu, B. Zhen, A. D. Stone, J. D. Joannopoulos, M. Soljačić, Bound states in the continuum. *Nat. Rev. Mater.* **1**, 16048 (2016).
50. B. A. Koscher, J. K. Swabeck, N. D. Bronstein, A. P. Alivisatos, Essentially trap-free $CsPbBr_3$ colloidal nanocrystals by postsynthetic thiocyanate surface treatment. *J. Am. Chem. Soc.* **139**, 6566–6569 (2017).

51. S. Yang, Y. Wang, P. Liu, Y.-B. Cheng, H. J. Zhao, H. G. Yang, Functionalization of perovskite thin films with moisture-tolerant molecules. *Nat. Energy* **1**, 15016 (2016).
52. G. Nedelcu, L. Protesescu, S. Yakunin, M. I. Bodnarchuk, M. J. Grotevent, M. V Kovalenko, Fast anion-exchange in highly luminescent nanocrystals of cesium lead halide perovskites ($CsPbX_3$, X= Cl, Br, I). *Nano Lett.* **15**, 5635–5640 (2015).
53. D. Magde, R. Wong, P. G. Seybold, Fluorescence quantum yields and their relation to lifetimes of rhodamine 6G and fluorescein in nine solvents: Improved absolute standards for quantum yields. *Photochem. Photobiol.* **75**, 327–334 (2002).
54. T. J. Whitcher, J.-X. Zhu, X. Chi, H. Hu, D. Zhao, T. C. Asmara, X. Yu, M. B. H. Breese, A. H. C. Neto, Y. M. Lam, Importance of electronic correlations and unusual excitonic effects in formamidinium lead halide perovskites. *Phys. Rev. X* **8**, 21034 (2018).
55. M. Humar, S. Hyun Yun, Intracellular microlasers. *Nat. Photonics* **9**, 572–576 (2015).
56. R. J. Elliott, Intensity of optical absorption by excitons. *Phys. Rev.* **108**, 1384–1389 (1957).
57. M. Saba, M. Cadelano, D. Marongiu, F. Chen, V. Sarritzu, N. Sestu, C. Figus, M. Aresti, R. Piras, A. G. Lehmann, Correlated electron–hole plasma in organometal perovskites. *Nat. Commun.* **5**, 5049 (2014).
58. R.-M. Ma, R. F. Oulton, Applications of nanolasers. *Nat. Nanotechnol.* **14**, 12–22 (2019).
59. S. I. Azzam, A. V Kildishev, R.-M. Ma, C.-Z. Ning, R. Oulton, V. M. Shalaev, M. I. Stockman, J.-L. Xu, X. Zhang, Ten years of spasers and plasmonic nanolasers. *Light Sci. Appl.* **9**, 90 (2020).
60. E. K. Keshmarzi, R. N. Tait, P. Berini, Single-mode surface plasmon distributed feedback lasers. *Nanoscale* **10**, 5914–5922 (2018).
61. M. Ramezani, A. Halpin, A. I. Fernández-Domínguez, J. Feist, S. R.-K. Rodriguez, F. J. Garcia-Vidal, J. G. Rivas, Plasmon-exciton-polariton lasing. *Optica* **4**, 31–37 (2017).
62. Y.-H. Chou, Y.-M. Wu, K.-B. Hong, B.-T. Chou, J.-H. Shih, Y.-C. Chung, P.-Y. Chen, T.-R. Lin, C.-C. Lin, S.-D. Lin, High-operation-temperature plasmonic nanolasers on single-crystalline aluminum. *Nano Lett.* **16**, 3179–3186 (2016).
63. A. E. Siegman, *An Introduction to Lasers and Masers* (McGraw-Hill, 1971).
64. H. Haug, S. Schmitt-Rink, Electron theory of the optical properties of laser-excited semiconductors. *Prog. Quantum Electron.* **9**, 3–100 (1984).
65. H. Deng, G. Weihs, D. Snoke, J. Bloch, Y. Yamamoto, Polariton lasing vs. photon lasing in a semiconductor microcavity. *Proc. Natl. Acad. Sci. U.S.A.* **100**, 15318–15323 (2003).